POLITECNICO DI MILANO
Scuola di Ingegneria Industriale e dell'Informazione
Corso di Laurea Magistrale in Ingegneria Aeronautica

Modelling aspects of wall flows with turbulent drag reduction

Relatore: Prof. Maurizio QUADRIO
Correlatore: Ing. Samuele ZAMPINI

Tesi di Laurea di:
Ilaria DE DOMINICIS, Matr. 770167

Anno Accademico 2013-2014

Alla mia famiglia

Ringraziamenti

Ringrazio di cuore il mio relatore, il Professor Quadrio, per tutto quello che mi ha insegnato, lavorare al suo fianco è stato davvero un onore, e il mio correlatore Samuele, per i saggi consigli, la disponibilità e per tutto l'entusiasmo che ha saputo trasmettermi.

Ringrazio tutta la mia famiglia, in particolare i miei genitori per avermi sostenuto in questi anni, per avermi sempre messo al primo posto e dato il meglio e le mie cugine per essere state le sorelle che non ho avuto.

In questi anni a Milano ho incontrare persone speciali che sono certa resteranno per sempre nella mia vita: Mirko, amico sempre pronto ad ascoltarmi, a bacchettarmi e allo stesso tempo a riempirmi di complimenti, grazie di esserci sempre stato, Benny, la coinquilina e l'amica migliore che si possa chiedere, Martina, Sergio, Alberto, Claudio, Carolina, Graziana, Peppe, Michela, Dalma, Francesca e tutti gli altri.

Infine desidero ringraziare il Professor Guardone per avermi incoraggiata a intraprendere un'esperienza all'estero che mi ha cambiato la vita e il Professor Boffadossi per tutti i suoi preziosi consigli.

Abstract

The performance of the turbulent drag reduction control techniques at application-level value of Reynolds number Re is an open question, since the methods employed so far in their assessment are limited to low values of Re. The goal of the present work is to understand whether and how turbulence models can predict skin-friction drag reduction induced by wall forcing. A plane channel flow controlled by a steady streamwise distribution of spanwise velocity is studied via Reynolds Averaged Navier-Stokes equations (RANS), by using two different turbulence models. Despite the quantitatively incorrect predictions, both turbulent models achieve a decrease of the skin friction drag. A preliminary analysis of the budget equations for the modelled quantities is used to investigate the process by which the physics of turbulent drag reduction can be captured by a simple RANS turbulence model.

Keywords: RANS, drag reduction, plane channel flow, turbulent flow

Sommario

Le prestazioni delle tecniche di controllo di riduzione di attrito in flussi turbolenti a valori applicativi del numero di Reynolds Re sono ad oggi sconosciute, in quanto le tecniche usate per studiarle sono limitate a valori bassi di Re. L'obbiettivo del lavoro è capire se e come i modelli di turbolenza possono predire la riduzione di attrito generata da un forzamento a parete. Una corrente in un canale piano forzato tramite una distribuzione stazionaria della componente trasversale della velocià a parete, modulata nella direzione longitudinale, è stato studiato tramite RANS usando due differenti modelli di turbolenza. Nonostante le previsioni siano quantitativamente non corrette, entrambi i modelli di turbolenza mostrano una diminuzione della resistenza d'attrito. Un'analisi preliminare delle equazioni di bilancio per le quantità modellate è effettuata per indagare il processo tramite il quale la fisica della turbolenza possa essere catturata da un semplice modello di turbolenza RANS.

Parole chiave: RANS, riduzione di turbolenza, flusso in un canale piano, flussi turbolenti

Estratto della tesi in lingua italiana

Le tecniche di controllo finalizzate a ridurre l'attrito in un flusso turbolento di parete sono un argomento di ricerca molto importante nel campo della fluidodinamica moderna. In tutti i sistemi caratterizzati da flussi turbolenti come oleodotti, pale di turbine o velivoli dalle elevate velocità, è possibile ottenere una diminuzione della potenza necessaria, quindi un miglioramento dell'efficienza, anche a partire da un'esigua riduzione dell'azione viscosa dovuta alla turbolenza.

I metodi di controllo si dividono in tecniche di tipo attivo (se è richiesta potenza esterna) o passivo, e in tecniche a ciclo aperto (se la legge di controllo è stabilita e non modificabile) o a ciclo chiuso. Sono state sviluppate varie strategie di controllo attive e a ciclo aperto con l'obiettivo di ridurre l'attrito in flussi turbolenti, infatti le prestazioni ottenute tramite tecniche di controllo passivo non sono considerevoli, ad esempio con le *riblets* [16] è stato calcolata una riduzione di resistenza pari a circa il 2% durante una prova di volo [41], mentre le tecniche di controllo in ciclo chiuso sono attualmente impraticabili in quanto complesse e di difficile implementazione.

In questo lavoro sono trattate solo le tecniche di controllo della turbolenza attive e a ciclo aperto basate sull'imposizione di un movimento della parete nel suo piano e la riduzione di attito è quantificata a partire dalla riduzione del valore del coefficiente d'attrito C_f nel caso forzato rispetto a quello di riferimento. Il metodo della *parete oscillante* è stato introdotto da Jung *et al.* [21], i quali si sono serviti dell'osservazione di Bradshaw e Pontikos [6] per cui un improvviso gradiente trasversale di pressione genera un calo temporaneo delle quantità turbolente. La massima riduzione d'attrito ottenuta con questa tecnica è 45%. Successivamente sono state proposte da Zhao *et al.* [44] le *onde viaggianti trasversalmente* a partire dal controllo tramite forza di volume non uniforme nello spazio studiato da Du e Karniadakis [12] e da Du, Symeonidis e Karniadakis [13]. Le prestazioni ottenute da questo tipo di forzamento in termini di riduzione di attrito sono però inferiori rispetto al metodo della parete oscillante [43]. Quadrio, Ricco and Viotti in [34] hanno introdotto le *onde viaggianti longitudinalmente* in cui si ha una modulazione della componente trasversale di velocità a parete, sia nel tempo che nella direzione longitudinale, e il caso particolare in cui la frequenza di oscillazione è nulla corrisponde alle onde stazionarie studiate da Viotti, Quadrio e Luchini in [40] mentre il caso particolare in cui è nullo il numero d'onda corrisponde alla parete oscillante. Le onde viaggianti longitudinalmente sono piuttosto promettenti: a $Re_\tau = 200$ la massima riduzione di resistenza ottenuta è pari al 52% se i paramenti del forzamento sono scelti in modo ottimale dal punto di vista della riduzione della turbolenza. Sfortunatamente fino ad oggi non è stato possibile indagare le prestazioni ottenibili da questa tecnica a valori applicativi del numero di Reynolds in quanto gli strumenti usati, ovvero Direct Numerical Simulation (DNS) ed esperimenti, sono limitati a valori bassi del numero di Reynolds. Questo vuol dire che è possibile ottenere buone prestazioni ad alti valori di Reynolds se i parametri del forzamento sono scelti in modo opportuno.

I pochi studi condotti a valori relativamente alti del numero di Reynolds mostrano che le prestazioni del controllo diminuiscono piuttosto rapidamente all'aumentare di tale valore, se i parametri del forzamento corrispondono a quelli ottimi per bassi valori del numero di Reynolds. Gatti and Quadrio [17] hanno già effettuato uno studio DNS parametrico completo a $Re_\tau = 2100$ considerando diversi valori del numero d'onda e della frequenza d'onda. Il quadro che emerge è che, aumentando il numero di Reynolds, le prestazioni diminuiscono in maniera fortemente dipendente dai parametri del controllo, i cui valori ottimi non sono costanti al variare del numero di Reynolds.

Una valida possibiltà che consente di studiare correnti caratterizzate da numeri di Reynolds alti sono le RANS. Fino ad ora nessun tentativo è stato fatto, dunque la capacità dei modelli di turbolenza di considerare un forzamento a parete non è nota. In questo lavoro è studiato l'effetto di un forzamento stazionario applicato ad un flusso turbolento in un canale piano tramite due modelli di turbolenza: il modello Launder Sharma $k-\epsilon$ e il modello $\overline{v^2}-f$. Entrambi i modelli adottano l'ipotesi di Boussinesq. Il Launder Sharma $k-\epsilon$ è stato ottenuto modificando il modello $k-\epsilon$ per mezzo di *funzioni di smorzamento* in modo da poter integrare le equazioni fino a parete.

Il modello $\overline{v^2} - f$ oltre alle due equazioni di bilancio per ϵ e per k richiede la soluzione di due equazioni aggiuntive: una di trasposto del termine v^2 e un'equazione ellittica di rilassamento.

La geometria e il tipo di forzamento sono scelte sulla base della semplicità. Il software OpenFOAM è utilizzato per la soluzione numerica delle equazioni discretezzate con il metodo dei volumi finiti. La mesh è generata tramite *blockMesh*. La direzione trasversale z è stata discretizzata con una sola cella in modo da effettuare una simulazione bidimensionale, l'imposizione di condizioni simmetriche al centro del canale ha consentito lo studio solo di metá dello stesso dimezzando il costo computazionale e condizioni periodiche sono utilizzate per l'implementazione pratica del dominio di calcolo infinito. Il numero di condizioni iniziali e il tipo di condizioni al contorno da imporre dipendono di modello di turbolenza utilizzato.

Le simulazioni sono condotte a $Re_\tau = 200$ e $Re_\tau = 1000$ in modo da poter quantificare l'errore commesso rispetto ai dati disponibili da studi DNS. Entrambi i modelli forniscono buoni risultati nel caso senza forzamento, con un errore percentuale massimo dell'ordine del 10%. Si osserva che nel caso di riferimento il valore del C_f calcolato è sempre minore rispetto a quello atteso. Nel caso forzato si ottiene una riduzione del C_f che, sebbene sia diversa di quella teorica, lascia intravedere la possibilità di studiare le tecniche di controllo di riduzione delle turbolenza tramite forzamento a parete via RANS.

Il meccanismo tramite il quale il modello di turbolenza riesce a catturare la fisica della riduzione di resistenza viene indagato tramite un'analisi delle equazioni di bilancio per l'energia cinetica media e turbolenta. Queste, dopo essere state mediate nelle direzioni omogenee z, t e nella direzione x quindi integrate nella direzione y, risultano essere molto semplici in quanto la geometria e il tipo di forzamento scelto consentono di eliminare molti termini perchè matematicamente nulli o empiricamente trascurabili. Sommando i termini rimanenti si ottiene l'equazione globale di bilancio per l'energia cinetica totale nella quale emerge il ruolo fondamentale della viscosità turbolenta ϵ. L'equazione di bilancio per questa quantità, fortemente coinvolta nella modellazione, viene studiata: si osserva che il termine di produzione di ϵ è un termine dominante che viene modificato molto dal forzamento. Questo è ottenuto come somma di due termini: uno direttamente legato al forzamento, l'altro indirettamente.

È stato possibile effettuare un'analisi quantitativa dei risultati disponendo di dati ottenuti tramite simulazioni DNS. L'errore percentuale commesso dalle RANS è moderato nel caso di riferimento non controllato, ma gli errori sono significativi nel caso forzato. La dissipazione viscosa ϵ è calcolata in maniere inaccurata. Tuttavia quando la giusta scalatura è usata per la ϵ calcolata con il modello $\overline{v^2} - f$ si osserva un andamento modulato in direzione x che è qualitativamente corretto anche se, oltre alla differenza numerica, si osservano delle differenze nella zona in cui il valore massimo viene raggiunto e nella forma che mostra un prolngamento nel caso DNS nella direzione del flusso. In conclusione si può affermare che i modelli di turbolenza sono in grado di considerare gli effetti del forzamento a parete, tuttavia in modo quantitativamente inaccurato. In particolare è rilevante l'errore nella modellazione della dissipazione turbolenta ϵ. Sarebbe interessante prendere in considerazione i modelli di turbolenza degli sforzi di Reynolds, ritenuti piú adatti allo studio di fenomeni fisici complessi.

Contents

1 Introduction **1**

2 Wall-based spanwise forcing **5**

- 2.1 Spanwise oscillating wall . . . 5
- 2.2 Spanwise-travelling waves . . . 6
- 2.3 Streamwise-travelling waves . . . 7
- 2.4 Stationary wall forcing . . . 8
- 2.5 Stokes layers . . . 9
  - 2.5.1 Temporal Stokes Layer (TSL) . . . 10
  - 2.5.2 Spatial Stokes Layer (SSL) . . . 10
  - 2.5.3 Generalized Stokes Layer (GSL) . . . 11
- 2.6 Reynolds number effect . . . 11

3 RANS equations **15**

- 3.1 Reynolds-Averaged Navier-Stokes equations . . . 15
  - 3.1.1 Launder Sharma $k - \epsilon$ model . . . 18
  - 3.1.2 $\overline{v^2} - f$ model . . . 20

4 The plane channel flow and OpenFOAM **23**

- 4.1 Averaging operators . . . 23
- 4.2 Flow configuration . . . 24
- 4.3 Numerical solution . . . 27
  - 4.3.1 Generation of the Mesh . . . 28
  - 4.3.2 Boundary conditions . . . 30
  - 4.3.3 Residuals . . . 33

5 Results **35**

- 5.1 DNS . . . 35

5.1.1 Skin Friction Coefficient 36
5.1.2 Mechanism of drag reduction 36
5.2 $\overline{v^2} - f$ model 46
5.2.1 Mechanism of drag reduction 46
5.3 Launder Sharma $k - \epsilon$ model 54
5.3.1 Prediction of drag reduction 56

6 Conclusions and Future Works **65**

List of Acronyms

CFD Computational Fluid Dynamics

DNS Direct Numerical Simulation

GSL Generalized Stokes Layer

LES Large Eddy Simulation

MKE Mean Kinetic Energy

RANS Reynolds Averaged Navier-Stokes equations

RSTM Reynolds Stress Transport Model

SI International System of Units

SSL Spatial Stokes Layer

TKE Turbulent Kinetic Energy

TSL Temporal Stokes Layer

List of Figures

1.1 Sketch of the turbulent channel flow with wall streamwise-travelling waves by Quadrio, Ricco and Viotti [34] 2

2.1 Map of friction R (%) for $A^+ = 12$ and $Re_\tau = 200$ by Quadrio *et al.* [34] 8

2.2 Experimental realization by Auteri *et al.* [2] 8

2.3 Literature data for maximum drag reduction rate R_m versus Re_τ by Gatti and Quadrio [17]. The solid line is $R_m \sim {Re_\tau}^{-0.2}$ 12

2.4 Sketch of the changes in drag reduction at different values of Reynolds number: low-*Re* on the left and high-*Re* on the right by Gatti and Quadrio [17] 13

2.5 Percentage drag reduction rate 100R versus ω^+ by Gatti and Quadrio [17] 13

5.1 Field of the spanwise velocity component W calculated via DNS 37

5.2 Energy Box: DNS at $Re_\tau = 200$. The two boxes represent Mean Kinetic Energy (MKE) and Turbulent Kinetic Energy (TKE). The quantities are scaled by the power $P_{,0_{DNS}}$ spent to drive the flow in the streamwise direction in the uncontrolled flow. 42

5.3 Energy Box: DNS at $Re_\tau = 200$. The two boxes represent MKE and TKE. The portion of MKE-x and of MKE-z indicate the portion of the MKE balance pertaining respectively to the streamwise and spanwise direction. The terms in the uncontrolled case are indicated by black portion of arrows, whereas the energy transfers due to the forcing are represented by red arrow or portion of arrows. The quantities are scaled by the power $P_{,0_{DNS}}$ spent to drive the flow in the streamwise direction in the uncontrolled flow. 43

5.4 Field of the turbulent dissipation ϵ^* calculated via DNS . . . 44

5.5 Section of the turbulent dissipation ϵ^* field calculated via DNS 44

5.6 Isosurfaces for the quantity $\lambda_2^+ = -0.03$ with DNS in the forced case coloured with the spanwise component of the velocity. 45

5.7 Energy Box: $\overline{v^2} - f$ model at $Re_\tau = 200$. The quantities are scaled by the power $P_{,0_{DNS}}$ spent to drive the flow in the streamwise direction in the uncontrolled flow calculated via DNS. 48

5.8 Turbulent viscous dissipation $\langle\epsilon\rangle^*_{zt}$ with $\overline{v^2} - f$ model at $Re_\tau =$ 200: reference case (top) and forced case (below). 50

5.9 Turbulent viscous dissipation $\langle\epsilon\rangle^*_{zt}$ with $\overline{v^2} - f$ model at $Re_\tau =$ 200: difference between the forced and the reference case. . . . 50

5.10 Turbulent dissipation budget with $\overline{v^2} - f$ model at $Re_\tau = 200$: terms in Eq. (5.29) averaged along x-direction. Reference case (thin lines) and forced case (thick lines). 51

5.11 Production terms of $\langle\epsilon\rangle_{zt}$, calculated with $\overline{v^2} - f$ model at $Re_\tau = 200$, averaged in x-direction in (5.32). Reference case (thin lines) and forced case (thick lines). 52

5.12 Energy Box: Percentage error committed by $\overline{v^2} - f$ at $Re_\tau = 200$. 54

5.13 Qualitative comparison between a section of the turbulent dissipation field ϵ^* calculated with DNS (top) and the averaged one $\langle\epsilon^*\rangle_{zt}$ calculated with $\overline{v^2} - f$ model (bottom). 55

5.14 Qualitative comparison between the Spatial Stokes Layer (SSL) calculated with DNS and the one calculated with $\overline{v^2} - f$ model. 55

5.15 Energy Box calculated with Launder Sharma $k - \epsilon$ model at $Re_\tau = 200$. 56

5.16 Turbulent viscous dissipation $\langle\epsilon\rangle_{zt}^{*}$ with Launder Sharma $k-\epsilon$ model at $Re_\tau = 200$: comparison between reference case (top) and forced one (bottom) 57
5.17 Turbulent viscous dissipation $\langle\epsilon\rangle_{zt}^{*}$ with Launder Sharma $k-\epsilon$ model at $Re_\tau = 200$: difference between forced and reference case. 58
5.18 Turbulent dissipation with Launder Sharma $k-\epsilon$ model: difference of term $\langle D\rangle_{zt}$ between the forced and the reference case. 58
5.19 Turbulent dissipation budget with Launder Sharma $k-\epsilon$ model: terms of (5.36) averaged in x-direction. Reference case (thin lines) and forced case (thick lines). 59
5.20 Launder Sharma $k-\epsilon$ model. Production terms of $\langle\tilde{\epsilon}\rangle_{zt}$ averaged in x-direction. Reference case (thin lines) and forced case (thick lines). 60
5.21 Energy Box: Percentage error committed by Launder Sharma $k-\epsilon$ at $Re_\tau = 200$. 61
5.22 Qualitative comparison between a section of the turbulent dissipation field ϵ^* calculated with DNS (top) and the averaged one $\langle\epsilon^*\rangle_{zt}$ calculated with Launder Sharma $k-\epsilon$ model (bottom). 62
5.23 Qualitative comparison between the SSL calculated with DNS and the one calculated with Launder Sharma $k-\epsilon$ model. . . 63

List of Tables

3.1 Launder Sharma $k - \epsilon$ model: Constants and Functions 19
3.2 $\overline{v^2} - f$ model: Constants and Functions 21

4.1 Computational domain size and spatial resolution for two sets of simulations carried out at different values of the friction Reynolds number Re_τ 25

5.1 Values and errors of the skin friction coefficient $\langle C_f \rangle_{xzt}$, in the reference and in the forced case, at $Re_\tau = 200$ and $Re_\tau = 1000$ achieved using the $\overline{v^2} - f$ model. 46
5.2 Values and errors of the skin friction coefficient $\langle C_f \rangle_{xzt}$ in the reference and in the forced case at $Re_\tau = 200$ and $Re_\tau = 1000$ with the Launder Sharma $k - \epsilon$ model. 56

Chapter 1

Introduction

One of the most challenging and important areas of fluid mechanics is the reduction of the skin-friction drag in fully developed turbulent wall flows. The growing interest in the subject lies in the significant role played by wall friction in the energy losses in a number of technological and industrial applications such as oil and gas pipelines, high-speed aircraft wings, jet engine intakes and turbine blades. Considerable improvements in terms of performance and fuel consumption can be achieved even by a small reduction of turbulent skin friction.

The control strategies are mainly grouped into passive (i.e. do not require energy to work) and active techniques, as well as open-loop (i.e. do not need sensors and a control law with feedback) and closed-loop techniques. Since passive techniques have achieved limited performance[1] and closed-loop techniques are today still impractical, various active open-loop techniques have been developed with the aim of reducing drag in fully developed turbulent flow. One interesting strategy currently under active study is the streamwise-travelling waves concept, introduced by Quadrio, Ricco and Viotti in [34]. The forcing consists in sinusoidal waves of spanwise velocity which vary in time t and are modulated in space along the streamwise direction x:

$$W = A\sin(\kappa_x x - \omega t), \tag{1.1}$$

where A is the forcing amplitude, $\kappa_x = 2\pi/\lambda_x$ is the streamwise wavenumber and $\omega = 2\pi/T$ is the oscillation frequency. The sign of the phase speed

---

[1] For example riblets [16] yield reduction of total aerodynamic drag of at least 2% in flight conditions [41].

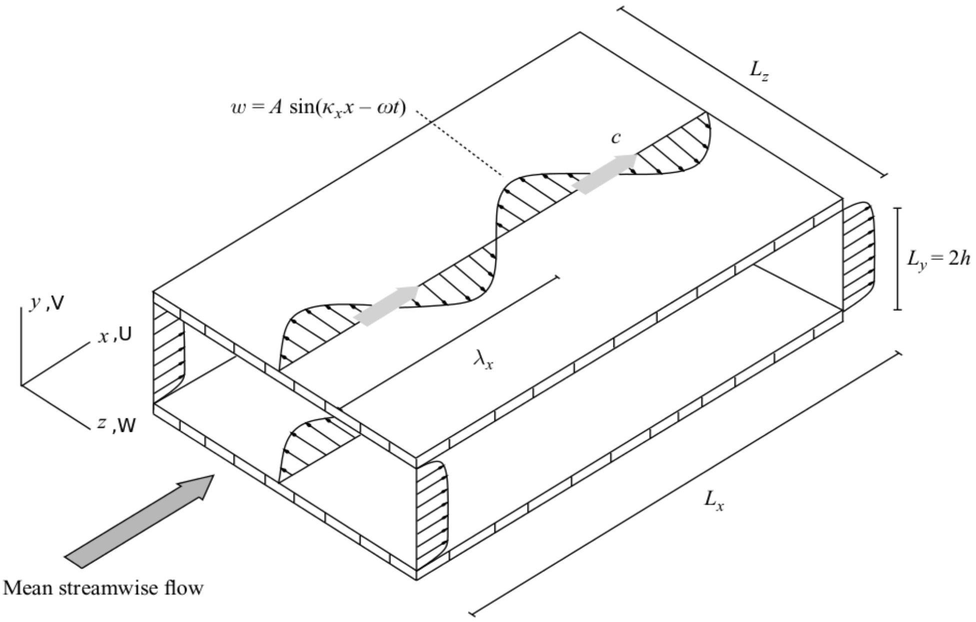

Figure 1.1: Sketch of the turbulent channel flow with wall streamwise-travelling waves by Quadrio, Ricco and Viotti [34]

$c = \omega/\kappa_x$ discriminates between forward- and backward-travelling waves. Stationary waves and oscillating wall are limiting cases, obtained respectively for $\omega = 0$ and for $\kappa_x = 0$.

Several DNS studies have been carried out, as well as one experimental investigation by Auteri *et at.* [2]. Unfortunately, both these techniques are limited to low values of Reynolds number, owing to the enormous increase of the computational cost of DNS and the shrinking of the size of required sensors and actuators to be employed in a laboratory experiment.

The performance of these control techniques at high values of the Reynolds number is a fundamental problem: the few higher- Re available data, achieved with the parameters of the wall forcing set at their low-Re optimal value, show a relative quick decrease of drag reduction when Re is increased. Typically, how the performance of the forcing depends upon the value of the Reynolds number is quantified in the literature ([36], [7],[38], [27], [4]) through the exponent γ of a power law $R_m \sim Re_\tau^\gamma$ that links the maximum drag reduction rate R_m, achieved at a fixed forcing amplitude A^+ , to the value of Re_τ, the Reynolds number based on the friction velocity u_τ. Gatti and Quadrio in [17] have performed a DNS up to $Re_\tau = 2100$, considering several wavenumbers and frequencies at each value of Re. A marked dependence between the rate at which drag reduction deceases and the control parameters seems to exist, therefore a chance for positive net energy saving at high Reynolds numbers is given.

In order to reach applicative value of the Reynolds number, different proposal have been put forward, for example the linearized studies of Moarref and Jovanović [27](which however required a DNS database for a non-manipulated flow and is thus useles in the present work) and Duque-Daza, Baig, Lockerby, Chernyshenko and Davies [14] or the perturbation analysis of the Navier–Stokes equations for the plane channel flow carried out by Belan and Quadrio [4]. Nowadays RANS simulations have not been carried out.

The objective of the present work is to understand whether and how the turbulence models can include drag reduction effects generated by a wall based forcing. A simulation of an incompressible fully developed turbulent channel flow altered by a wall forcing, consisting of a steady distribution of spanwise velocity, modulated in the streamwise direction, is performed via RANS. This flow configuration is chosen as the simplicity of the plane channel makes it one of the best prototypes to understand turbulent phenomena and the steady forcing is one of the easiest drag reduction techniques. The focus is on how the forcing affects the energy transfer between the mean flow and the turbulent fluctuations. In particular is investigated the viscous dissipation ϵ that is an quantity deeply involved in the modelling. A quantitative analysis of the results is possible starting from the DNS data.

The numerical solution is performed by means of OpenFOAM, a free, open-source numerical simulation software with extensive Computational Fluid Dynamics (CFD) and multi-physics capabilities.

In this paper, x, y and z are used to indicate the streamwise, wall-normal and spanwise coordinates; the respective velocity components are U, V and W. The subscript 0 refers to uncontrolled flow. The superscript $+$ indicates non-dimensional quantities scaled by the cinematic viscosity of the fluid ν and the friction velocity $u_{\tau,0}$ of the uncontrolled flow, whereas superscript $*$ refers to quantities scaled by the channel half-width h and the centreline velocity of a laminar Poiseuille flow with the same flow rate U_p.

Chapter 2

Wall-based spanwise forcing

This chapter reviews the active open-loop drag reduction techniques based on the spanwise movement of the wall and the respective Stokes layers are shortly described. The effect of the Reynolds number is then discussed.

The energetic performance of the control strategies is here evaluated using the following quantities, introduced by Kasagi, Hasegawa and Fukagata in [22]:

- the *net energy saving* S

  $$S = \frac{P_0 - (P + P_{in})}{P_0}, \tag{2.1}$$

  where P is the power spent to drive the fluid along the streamwise direction and P_{in} is the power required to enforce the control action, considering ideal actuators.

- the *drag-reduction rate* R

  $$R = \frac{P_0 - P}{P_0}, \tag{2.2}$$

  equal to the reduction of the skin-friction coefficient C_f if the mass flow rate is constant.

2.1 Spanwise oscillating wall

The favourable modification of wall turbulence by spanwise wall-based forcing was first proposed by Bradshaw and Pontikos [6]. They have observed that a sudden spanwise pressure gradient generates a transient drop in turbulent friction, but if the pressure gradient is kept constant there is a recovery of it. Almost 20 years ago Jung *et al.* [21] and Akhavan *et al.* [1] have demonstrated that a significant turbulent drag reduction is achievable by spanwise pressure gradient harmonic in time or equivalently by harmonic oscillation of the wall. They have introduced the spanwise-oscillating wall technique:

$$W = A \sin(\omega t), \tag{2.3}$$

where A is the forcing amplitude and $T = 2\pi/\omega$ is the forcing period.

The analysis has been carried on in successive studies DNS-based and laboratory experiments ([8], [9]).

A maximum R as high as 45% is achievable once A and T are set within the optimum range from the R viewpoint, however a Quadrio and Baron [3] have demonstrated that a net energy saving $S \simeq 0.07$ is possible because the net energy saving R may offset the energy loss due to the forcing against the viscosity resistance of the flow. A qualitative explanation of this mechanism is that the interaction between traverse oscillating boundary layer, induced by wall motion, and the near-wall turbulent structures weakens the viscous wall cycle.

2.2 Spanwise-travelling waves

Du and Karniadakis [12] and Du, Symeonidis and Karniadakis [13] have first proposed a spanwise-travelling wave of spanwise body force:

$$F_z = I e^{-y/\Delta} \sin(\kappa_z z - \omega t), \tag{2.4}$$

where the intensity I has its maximum at the wall and exponentially decays away from it. The forcing is modulated in time and in the spanwise direction z where it can be described as a wave with wavelength $\lambda_z = 2\pi/\kappa_z$.

The limited number of parameter combinations considered in that study makes the study non conclusive, nevertheless the flow visualizations clearly show significant modifications of the near-wall flow structures: the wall-streak instability can be stabilized leading to the suppression of the turbulence production and to large amounts of drag reduction.

Zhao *et al.* [44] translated the forcing (2.4) into a space-time distribution of wall velocity:

$$W = A \sin(\kappa_z z - \omega t). \tag{2.5}$$

They have carried out only two simulations, reaching similar results in terms of drag reduction and flow statistics compared to the waves of body force, but negative values of the net energy saving S have been found. Later, Xie [43] demonstrated and explained that the energy performance achievable by this kind of forcing is always worse compared with the oscillating wall technique.

2.3 Streamwise-travelling waves

They have been introduced by Quadrio, Ricco and Viotti in [34]. The forcing consists of waves of spanwise velocity moving in the streamwise direction:

$$W = A \sin(\kappa_x x - \omega t). \tag{2.6}$$

A large DNS-based parametric study, at fixed $A^+ = 12$ and $Re_\tau = 200$ has been carried out in order to explore the dependence of the drag reduction on the forcing parameters over the entire $\kappa_x - \omega$ plane. The limiting case for κ_x or ω equal to zero correspond respectively to the oscillation wall and the stationary waves. As shown in the Fig (2.1) the effects of the travelling waves, in terms of the percentage change in friction drag, as function of κ_x and ω are not trivial: backward travelling waves always produce drag reduction, whereas forward travelling waves, depending on the speed of the waves, can produce both a large drag reduction as well as a drag increase. An extremely good occurrence is that the region of minimum P_{in} almost coincides with the region of maximum drag reduction. If $\omega \approx 0.15$ and $\kappa_x \approx 1$ the maximum value of the net energy saving S, equal to $18,\%$ is measured.

An experimental confirmation of the above results have been reported by Auteri *et al.* [2]. They have built a circular pipe where the travelling waves are generated by independent azimuthal oscillation of thin axial pipe slabs as shown in Fig.(2.2). A Fourier analysis has revealed that the discrete spatial waveform, inevitably used in the experiment, need to be accounted for, since it is responsible for significant effects that are absent in DNS studies.

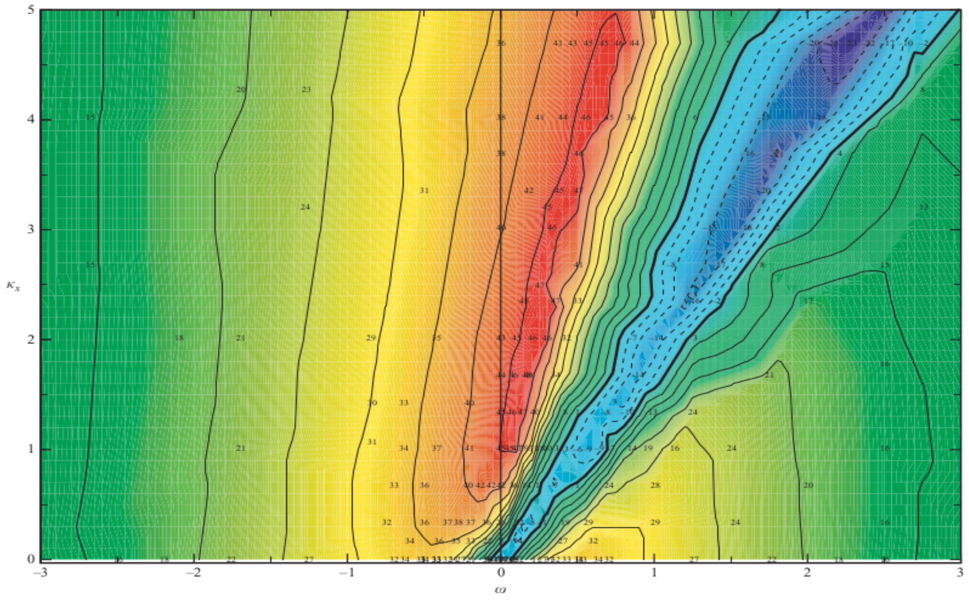

Figure 2.1: Map of friction R (%) for $A^+ = 12$ *and* $Re_\tau = 200$ *by Quadrio* et al. *[34]*

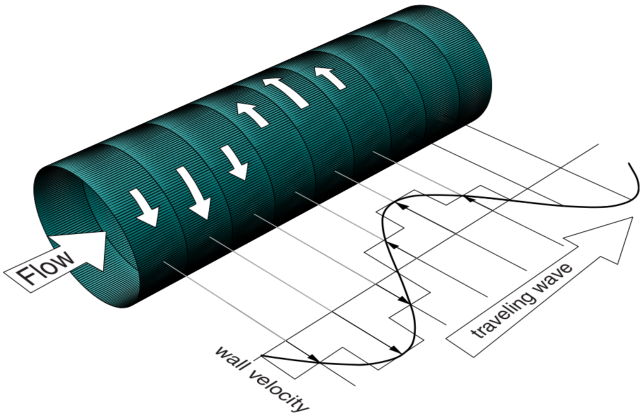

Figure 2.2: Experimental realization by Auteri et al. *[2]*

2.4 Stationary wall forcing

Viotti, Quadrio and Luchini in [40] have translated the time-dependent forcing law expressed by (2.3) into a stationary formula

$$W = A\sin(\kappa_x x). \tag{2.7}$$

In this way they have got rid of one of the main drawbacks of the oscillating wall technique, i.e. its unsteady nature. The maximum R is up to 52% for the forcing amplitude $A^+ = 20$ and the forcing wavelength $\lambda_x^+ = 1250$ at $Re_\tau = 200$. The link between the two kinds of forcing is the convection velocity of the turbulent fluctuations $\mathscr{U}_w$. It resembles the mean velocity profile only in the bulk of the flow but near the wall, below $y^+ = 15$, it takes a well-defined non-zero value $\mathscr{U}_w \simeq 10$ as showed by Kim and Hussain in [23]. A similar space-time extension has been discussed by Berger*et al.* [5] where spanwise-oriented Lorenz volume force were simulated via DNS. However no conclusion can be drawn a priori because of the substantial difference between body force and wall-based forcing.

Temporal and spatial forcing show qualitative analogy: the forcing wavelength that yields the maximum value for drag reduction has been found to correspond to the optimal period of the oscillating wall, for all amplitudes. Differences exist from the point of view of energetic budget: the spacial forcing is more efficient both for absolute drag reduction rate R and net power saving S.

2.5 Stokes layers

The physics behind the drag reduction is based on interaction between the Stokes layer and the near wall turbulence. Quadrio and Baron in [3] have attempted to explain this mechanism as a phase shift between the low-speed streaks and the quasi-streamwise vortical structures whereas Choi, DeBisshop and Clyton in [8] as the creation of negative spanwise vorticity during the oscillation cycle.

In this section are addressed the three kind of Stokes layers, determined by the different boundary conditions imposed at the wall. For each of them, a laminar Poiseulle flow subject to a boundary forcing is first considered, therefore the laminar solution is compared to the turbulent flow, averaged in the homogeneous directions, and in all the cases the agreement has been found. A clear relation between R and the thickness of the Stokes layers exists if the phase speed of the waves is sufficiently different from the near wall turbulent convection velocity $\mathscr{U}_w$ and if the waves time scale, defined as $\mathscr{T} \equiv \frac{\lambda_x}{c - \mathscr{U}_w}$, is significantly smaller that the lifetime of the turbulent structures [31].

2.5.1 Temporal Stokes Layer (TSL)

When the forcing (2.3) is imposed at the wall of a laminar Poiseulle flow, the entire flow consists in a parabolic profile plus a spanwise alternating motion called Temporal Stokes Layer (TSL). The analytical expression of the TSL is known since it corresponds to the oscillating transversal boundary layer that develops in the second Stokes problem: an exact solution of Navier–Stokes equations for an incompressible laminar flow, where a still fluid is bounded by a wall subject to harmonic oscillation. The momentum equation reduces to:

$$\frac{\partial W}{\partial t} - \nu \frac{\partial^2 W}{\partial y^2} = 0 \tag{2.8}$$

with boundary conditions

$$W(0,t) = \begin{cases} 0 & t < 0 \\ \tilde{W} cos(\omega t) & t \geqslant 0 \end{cases} \tag{2.9}$$

and

$$W(\infty, t) = 0. \tag{2.10}$$

The analytical solution, function of the two independent variables (x,t), is:

$$\frac{W}{\tilde{W}} = e^{\sqrt{\frac{\omega}{2\nu}} y} cos\left(\omega t - \sqrt{\frac{\omega}{2\nu}} y\right), \tag{2.11}$$

2.5.2 Spatial Stokes Layer (SSL)

It is the spatial equivalent of the TSL, if a steady forcing (4.11) is imposed at the wall. The approximated analytical solution exists (see [40]) for a laminar Poiseuille flow under the assumption that the thickness of the SSL is much smaller that the channel half-height h:

$$W(x,y) = C_x \mathscr{R}\left[e^{i\kappa_x x} Ai\left(-\frac{iy}{\delta_x} e^{-i4/3\pi}\right)\right]. \tag{2.12}$$

In this expression C_x represents a normalization constant, $\kappa_x = 2\pi/\lambda_x$ is the forcing wavenumber and δ_x is the thickness of the SSL, defined as $\delta_x = \left(\frac{\nu}{u_{y,w}\kappa_x}\right)^{1/3}$ where $u_{y,w}$ is the gradient of the streamwise mean velocity profile evaluated at the wall.

It is a function of the two independent variables (x,y).

2.5.3 Generalized Stokes Layer (GSL)

Considering a laminar Poiseulle flow, subject to the boundary forcing (2.6), the analytical expression for the traverse boundary layer created by the waves, has been achieved by Quadrio and Ricco in [33] under the same hypothesis of the SSL. It is a function of the three independent variables (x,y,t):

$$W(x,y,t) = A\mathscr{R}\left\{ Ce^{\frac{2\pi i(x-ct)}{\lambda}} Ai\left[e^{\frac{\pi i}{6}} \left(\frac{2\pi u_{y,w}}{\lambda\nu}\right)^{\frac{1}{3}} \left(y - \frac{c}{u_{y,w}}\right)\right]\right\} \quad (2.13)$$

where C is a complex constant.

2.6 Reynolds number effect

The performance losses of the spanwise wall forcing at applicative values of the Reynolds number are a open issue: the available data, from DNS of experiments, concern mainly flow at very low values of Reynolds number. The few higher-Re data suggest a dependence of the performance of the forcing upon the value of the Reynolds number through a power law $R_m \sim {Re_\tau}^{\gamma}$, where R_m is the maximum drag reduction rate achievable at a fixed forcing amplitude A^+. The exact value of the exponent γ is not well defined: theoretical studies are not entirely in agreement with the empirical information. In Fig.(2.3) the literature data for maximum drag reduction rate R_m versus Re_τ are shown. The solid line is $R_m \sim {Re_\tau}^{0.2}$, black symbols refer to DNS studies whereas white symbols to experimental measurements. The value of the forcing amplitude varies in the different datasets as well as the kind of the forcing (circles: oscillating walls ([36], [37]); triangles: stramwise-travelling waves ([34], [2]); square: spanwise-travelling waves ([12], [13]) and diamonds: Lorenz force ([28], [5]).

Gatti and Quadrio in [17] have carried out a parametric survey up to $Re_\tau = 2100$ via DNS. They have found a compromise, between the computational cost and the need of time-averaging the fluctuating space-mean wall shear stress, adjusting the size of the computational domain in the homogeneous directions. Although the drag reduction can be lightly overestimated, the results are in accordance with the DNS data and when Re is increased a relatively quick decrease of the drag reduction is observed if the parameters

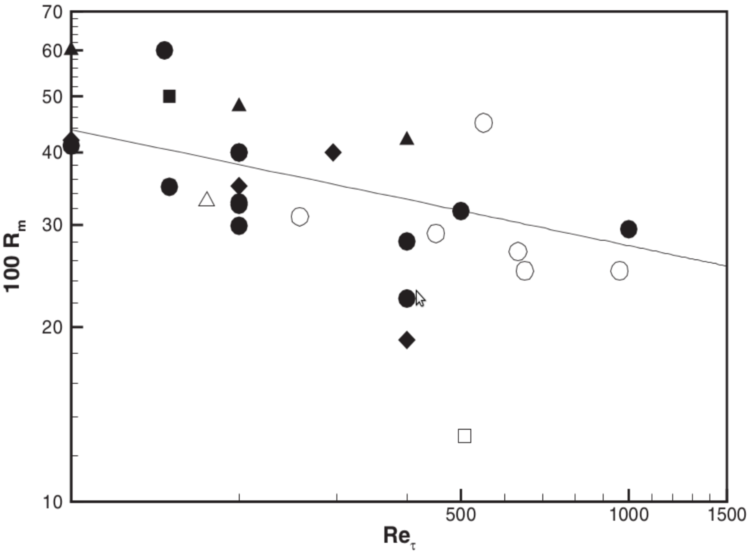

Figure 2.3: Literature data for maximum drag reduction rate R_m versus Re_τ by Gatti and Quadrio [17]. The solid line is $R_m \sim {Re_\tau}^{-0.2}$

of the forcing are kept at their low-Re optimal value. However the rate at which R drops markedly depends on the control parameters and for higher Re the optimal control parameters are shifted towards higher frequencies and wavenumbers. A similar result has been achieved by Hurst and Chung [10].

In the Fig. (2.4) is sketched the change in drag reduction in the ${\kappa_x}^+ - \omega^+$ plane when the Reynolds number is increased: the picture on the left refers to a low-Re case and the one on the right to a high-Re case. The value of the exponent γ is not constant when ${\kappa_x}^+$ and ω^+ are varied. In particular there are some regions that are less sensitive to Re: if $\omega^+ = 0.08$ and ${\kappa_x}^+ = 0.035$, γ is found to be equal to -0.1 thus a large values of R seems to be achievable also at high values of the Reynolds number.

The percentage drag reduction R, obtained by streamwise travelling waves with constant wavelength $\lambda^+ = 1250$ and $A^+ = 12$, is plotted versus ω^+ in Fig.(2.5). Since only steady forcing has been considered in this work, the error committed by the RANS simulations has been evaluated respect to the value corresponding to $\omega^+ = 0$: 45% at $Re_\tau = 200$ and 30% at $Re_\tau = 1000$.

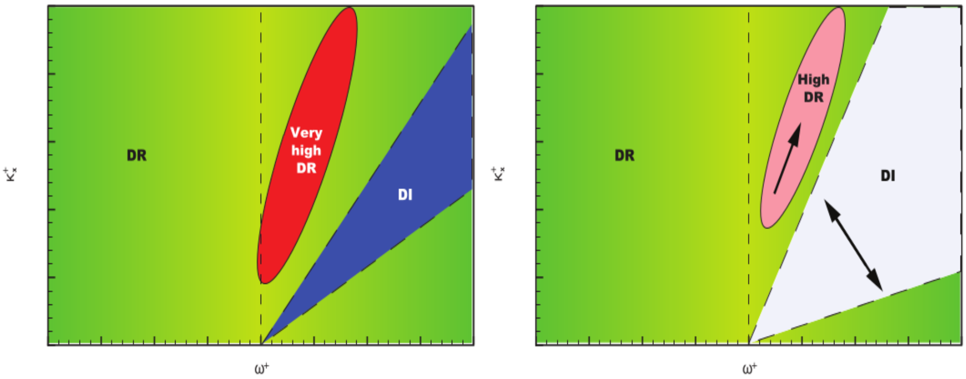
DR
Very high DR
DI
κ_x^+
ω^+
DR
High DR
DI
κ_x^+
ω^+

Figure 2.4: Sketch of the changes in drag reduction at different values of Reynolds number: low-Re on the left and high-Re on the right by Gatti and Quadrio [17]

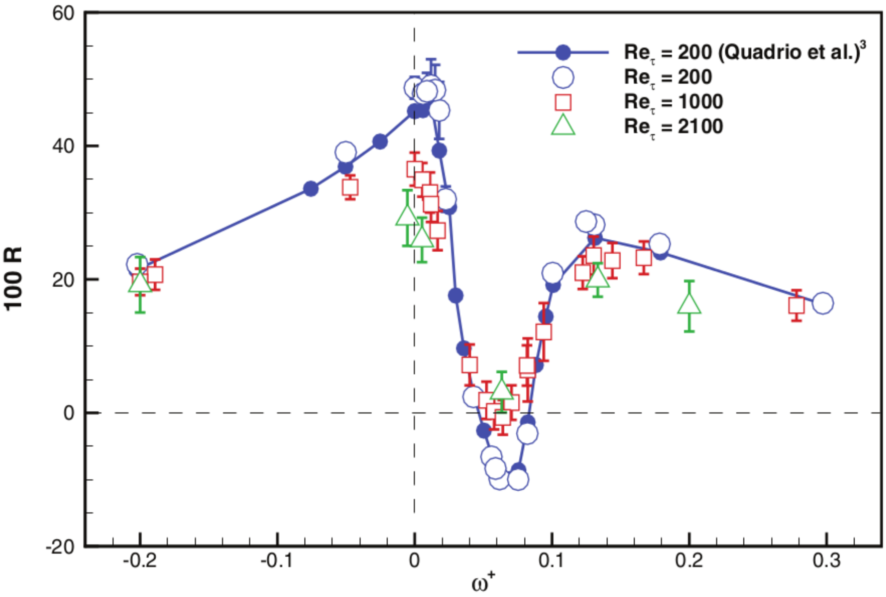

Figure 2.5: Percentage drag reduction rate 100R versus ω^+ by Gatti and Quadrio [17]

Chapter 3

RANS equations

In this chapter the RANS equations are introduced and the closure turbulence models used in this work are addressed.

3.1 Reynolds-Averaged Navier-Stokes equations

Different approaches to the numerical simulation of turbulent flows have been developed through them, RANS is a cost-effective means to study flows with high Reynolds numbers. The DNS of the Navier-Stokes equations, with appropriate initial and boundary conditions lead to the most detailed solution, but it requires the resolution of all the scales of motion. The computational cost increases with Re^3 limiting its application to low Reynolds numbers. Large Eddy Simulation (LES) is a compromise between DNS and RANS, however it is still expensive when applied to practical engineering problems.

The continuity and Navier-Stokes equations for a constant-proprieties Newtonian fluid flow, are given by:

$$\nabla \cdot \mathbf{U} = 0 \tag{3.1}$$

$$\frac{\partial \mathbf{U}}{\partial t} + \mathbf{U} \cdot \nabla \mathbf{U} = \frac{1}{\rho} \nabla p + \nu \nabla^2 \ \mathbf{U} \tag{3.2}$$

where $\mathbf{U}$ and p are respectively velocity and pressure.

The idea behind the RANS equations is the *Reynolds decomposition*, whereby an instantaneous quantity, for example velocity, is decomposed into its mean $\langle \mathbf{U}(\mathbf{x}) \rangle_t$ and the fluctuation $\mathbf{u}(\mathbf{x},\mathrm{t})$:

$$\mathbf{U}(\mathbf{x},t) = \langle \mathbf{U}(\mathbf{x}) \rangle_t + \mathbf{u}(\mathbf{x},t) \tag{3.3}$$

where

$$\langle \mathbf{U}(\mathbf{x}) \rangle_t = \lim_{T\to\infty} \frac{1}{T} \int_0^T \mathbf{U}(\mathbf{x},t)dt. \tag{3.4}$$

The equations (3.1) and (3.2) after the splitting of each instantaneous quantity (i.e $\mathbf{U}$ and p), by means of the Reynolds decomposition, and the time-averaging are:

$$\frac{\partial \langle U_j \rangle_t}{\partial x_j} = 0 \tag{3.5}$$

$$\langle U_i \rangle_t \frac{\partial \langle U_j \rangle_t}{\partial x_i} = \nu \frac{\partial^2 \langle U_j \rangle_t}{\partial x_i^2} - \frac{\partial \langle u_i u_j \rangle_t}{\partial x_i} - \frac{1}{\rho}\frac{\partial \langle p \rangle_t}{\partial x_j}. \tag{3.6}$$

Eq.(3.6) are called *Reynolds equations*. A manipulation of them yields:

$$\rho \langle U_i \rangle_t \frac{\partial \langle U_j \rangle_t}{\partial x_i} = \frac{\partial}{\partial x_i}\left[\mu\left(\frac{\partial \langle U_i \rangle_t}{\partial x_j} + \frac{\partial \langle U_j \rangle_t}{\partial x_i}\right) - \langle p \rangle_t \delta_{ij} - \rho \langle u_i u_j \rangle_t\right], \tag{3.7}$$

where the $\langle u_i u_j \rangle_t$ term can be interpreted as stress, the *Reynolds stress*. In fact the terms in the square brackets represent the sum of, respectively, the viscous stress, the isotropic stress and the Reynolds stress, pre multiplied by density since its conventional definition.

The Reynolds stresses are the component of a symmetric tensor, of which half of the trace is by definition the *turbulent kinetic energy*

$$\langle k \rangle_t = \frac{1}{2} \langle u_i u_i \rangle_t , \tag{3.8}$$

whereas the *dissipation rate of turbulent kinetic energy* ϵ is defined as

$$\langle \epsilon \rangle_t = \nu \left\langle \frac{\partial u_j}{\partial x_i}\frac{\partial u_j}{\partial x_i} \right\rangle_t . \tag{3.9}$$

Taking the divergence of Eq.(3.6) yields a Poisson's equation for the mean pressure $\langle p \rangle_t$:

$$-\frac{1}{\rho}\frac{\partial^2 \langle p \rangle_t}{\partial x_i^2} = \left\langle \frac{\partial U_i}{\partial x_j}\frac{\partial U_j}{\partial x_i} \right\rangle_t . \tag{3.10}$$

The four independent equations governing the mean velocity field (i.e the continuity equation - or, alternatively, Poisson's equation - and the 3 scalar Reynolds equations) are not enough to solve the problem, since these equations contain more than four unknowns: $\langle p\rangle_t$, $\langle \mathbf{U}\rangle_t$ and $\langle u_i u_j\rangle_t$. This leads to the closure problem. In order to solve the Reynolds equations the Reynolds stresses have to be determined by means of a turbulence model.

Since the early 1950s two main categories of turbulence models had evolved:

Turbulent-viscosity hypothesis models

The turbulent viscosity models adopt the Boussinesq hypothesis based on the proportionality between Reynolds stresses and the local velocity gradients:

$$-\rho \langle u_i u_j\rangle_t + \frac{2}{3}\rho \langle k\rangle_t \delta_{ij} = 2\rho \langle \nu_T\rangle_t \left(\frac{\partial \langle U_i\rangle_t}{\partial x_j} + \frac{\partial \langle U_j\rangle_t}{\partial x_i}\right) \tag{3.11}$$

where the positive scalar coefficient $\langle \nu_T\rangle_t$ is the so called *eddy viscosity.* Substituting the Eq.(3.11) in the Eq.(3.6), the mean-momentum equations are obtained:

$$\langle U_i\rangle_t \frac{\partial \langle U_j\rangle_t}{\partial x_i} = \frac{\partial}{\partial x_i}\left[\langle \nu_{eff}\rangle_t \left(\frac{\partial \langle U_i\rangle_t}{\partial x_j} + \frac{\partial \langle U_j\rangle_t}{\partial x_i}\right)\right] - \frac{1}{\rho}\frac{\partial}{\partial x_j}(\langle p\rangle_t + \frac{2}{3}\rho k) \tag{3.12}$$

where

$$\langle \nu_{eff}(\mathbf{x},t)\rangle_t = \nu + \langle \nu_T(\mathbf{x},t)\rangle_t\,. \tag{3.13}$$

They are characterized by the same form of the steady Navier–Stokes equations, but $\langle U\rangle_t$, $\langle \nu_{eff}\rangle_t$ and $\langle p\rangle_t + \frac{2}{3}\rho\langle k\rangle_t$ appear in place of U, ν and p.

The turbulent viscosity hypothesis is based on a mathematical description of Reynolds stresses similar to the one describing the molecular gradient-diffusion process. But, since these two processes are based on different physical laws the turbulent viscosity hypothesis does not possesses a general validity. However, in case of simple shear flow the results obtained seem to be adequate and so this hypothesis is often reasonably accurate.

In order to calculate the eddy viscosity, once adopted the turbulent viscosity hypothesis, different models have been proposed, from the algebraic ones, suggested by Prandtl and also known as zero equation models, to the

n-equations models, where n is the number of equations to be solved in addition to conservation of mass and momentum equations for the mean flow.

Modelling the direct influence of viscosity in the near-wall region and the related difficulties can be avoided through the wall functions if the value of Reynolds number is high enough to minimize the viscous effect or to allow the establishment of the universal wall function. Otherwise the so called *low Reynolds number models* have to be employed. Those models are modified in order to describe a flow close to a solid wall, integrating the model equations right through the wall. Since Van Driest [39] has introduced the easiest damping function in 1956, various models, incorporating wall damping effect and/or molecular effect, have been developed [29].

Reynolds Stress Models

They are the most complex classical turbulence models and quantitative accuracy is often not easy to achieve [42]. They require a model transport equation for each Reynold stress component and for the dissipation $\langle \epsilon \rangle_t$. Those models are not studied in this work, even though they probably are more fitting to account for the wall forcing effect. In fact in contrast to eddy-viscosity models, this category of models accommodate, without the introduction of empirical terms, different effects such as sudden stain rate, streamline curvature, rigid body rotation and body force. Except for near wall treatments, generally no Reynolds number dependence has been observed.

In this work we use two low-Reynolds turbulence models of the first category, that are described below.

3.1.1 Launder Sharma $k - \epsilon$ model

It is a low-Reynolds turbulence model proposed by Launder and Sharma [24] in 1974, as a variant of the k-ϵ model. They have studied a flow in the vicinity of a spinning disc in order to predict swirling flows. The two equations of the model are:

$$\langle U_i \rangle_t \frac{\partial \langle k \rangle_t}{\partial x_i} = \frac{\partial}{\partial x_j} \left[\left(\nu + \frac{\langle \nu_T \rangle_t}{\sigma_K} \right) \frac{\partial k}{\partial x_j} \right] + \langle P_k \rangle_t - \langle \tilde{\epsilon} \rangle_t - \langle D \rangle_t \qquad (3.14)$$

$$\begin{aligned}\langle U_i\rangle_t \frac{\partial \langle\tilde{\epsilon}\rangle_t}{\partial x_i} &= \frac{\partial}{\partial x_j}\left[\left(\nu + \frac{\langle\nu_T\rangle_t}{\sigma_\epsilon}\right)\frac{\partial \langle\tilde{\epsilon}\rangle_t}{\partial x_j}\right] \\ &+C_{\epsilon 1} f_1 \frac{\langle\tilde{\epsilon}\rangle_t}{\langle k\rangle_t}\langle P_k\rangle_t - C_{\epsilon 2}\langle f_2\rangle_t \frac{{\langle\tilde{\epsilon}\rangle_t}^2}{\langle k\rangle_t} + \langle E\rangle_t ,\end{aligned} \tag{3.15}$$

where $\langle P_k\rangle_t$ is the production of turbulent kinetic energy

$$\langle P_k\rangle_t = -\langle u_i u_j\rangle_t \frac{\partial \langle U_i\rangle_t}{\partial x_j}. \tag{3.16}$$

The dissipation variable $\langle\tilde{\epsilon}\rangle_t = \langle\epsilon\rangle_t - \langle D\rangle_t$ is used, as Jones and Launder proposed in [20], because of its numerical convenience in imposing the boundary condition. The extra term $\langle E\rangle_t$ is used in the transport equation in order to improve prediction in the wall region.

The exact equation for the dissipation rate $\langle\epsilon\rangle_t$ could be derived but is best viewed as empirical because $\langle\epsilon\rangle_t$ is mainly determined by the large-scale motions whereas the exact equation pertains to processes in the dissipative range [30].

Then $\langle\nu_T\rangle_t$, that depends only on the turbulence quantities $\langle k\rangle_t$ and $\langle\epsilon\rangle_t$, is calculated as

$$\langle\nu_T\rangle_t = C_\mu \langle f_\mu\rangle_t \frac{{\langle k\rangle_t}^2}{\langle\epsilon\rangle_t}. \tag{3.17}$$

The values of the five adjustable constants, two extra terms $\langle D\rangle_t$ and $\langle E\rangle_t$ and three damping function contained in the equations are given in Table [3.1], where $\langle R_T\rangle_t = \frac{\langle k\rangle_t^2}{\nu\langle\tilde{\epsilon}\rangle_t}$.

$\langle f_\mu\rangle_t$	f_1	$\langle f_2\rangle_t$	$\langle E\rangle_t$
$exp\left[-\frac{3.4}{(1+\frac{\langle R_T\rangle_t}{50})^2}\right]$	1	$1-0.3exp(-{\langle R_T\rangle_t}^2)$	$2\nu\nu_T\left(\frac{\partial^2 U_i}{\partial x_i \partial x_k}\right)$

$\langle D\rangle_t$	C_μ	$C_{\epsilon 1}$	$C_{\epsilon 2}$	σ_k	σ_ϵ
$2\nu\left(\frac{\partial\sqrt{\langle k\rangle_t}}{\partial x_j}\right)^2$	0.09	1.44	1.92	1	1.3

Table 3.1: Launder Sharma $k-\epsilon$ model: Constants and Functions

The boundary conditions to be imposed at the wall are $\langle k\rangle_t = 0$ and $\langle\tilde{\epsilon}\rangle_t = 0$.

3.1.2 $\overline{v^2} - f$ model

It is a near-wall turbulence model, originally proposed by Durbin in 1991 [15], where the non-locality is represented by solving an elliptic relaxation equation for $\langle f \rangle_t$, the variance of the normal velocity adjacent to a wall is modelled through $\langle v^2 \rangle_t = \langle u_i u_j \rangle_t n_i n_j$ and there is no need for damping functions. Some modifications have been made by Lien and Kalitzin [25] in order to enhance the numerical stability by means of a segregated numerical procedure which does not allow an implicit coupling between $\langle v^2 \rangle_t$ and $\langle f \rangle_t$ at the wall, and later Davidson, Nielsen and Sveningsson [11] have imposed a limit on the turbulence viscosity.

The resulting equations consist of the two standard $k - \epsilon$ equations

$$\langle U_i \rangle_t \frac{\partial \langle k \rangle_t}{\partial x_i} = \frac{\partial}{\partial x_j} \left[\left(\nu + \frac{\langle \nu_T \rangle_t}{\sigma_K} \right) \frac{\partial \langle k \rangle_t}{\partial x_j} \right] + \langle P_k \rangle_t - \langle \epsilon \rangle_t \tag{3.18}$$

$$\langle U_i \rangle_t \frac{\partial \langle \epsilon \rangle_t}{\partial x_i} = \frac{\partial}{\partial x_j} \left[\left(\nu + \frac{\langle \nu_T \rangle_t}{\sigma_\epsilon} \right) \frac{\partial \langle \epsilon \rangle_t}{\partial x_j} \right] + \frac{\langle C_{\epsilon 1} \rangle_t \langle P_k \rangle_t - C_{\epsilon 2} \langle \epsilon \rangle_t}{\langle T \rangle_t}, \tag{3.19}$$

the $\langle v^2 \rangle_t$ transport equation

$$\begin{aligned} \langle U_i \rangle_t \frac{\partial \langle v^2 \rangle_t}{\partial x_i} &= \frac{\partial}{\partial x_j} \left[\left(\nu + \frac{\langle \nu_T \rangle_t}{\sigma_K} \right) \frac{\partial \langle v^2 \rangle_t}{\partial x_j} \right] \\ &+ min(\langle k \rangle_t \langle f \rangle_t , - \langle \alpha \rangle_t + C_2 \langle P_k \rangle_t) - 6 \frac{\langle \epsilon \rangle_t}{\langle k \rangle_t} \langle v^2 \rangle_t \end{aligned} \tag{3.20}$$

and the elliptic relaxation equation for $\langle f \rangle_t$

$$\langle L \rangle_t \frac{\partial^2 \langle f \rangle_t}{\partial x_j x_j} = \langle f \rangle_t - \frac{1}{\langle k \rangle_t} \left[\langle \alpha \rangle_t - C_2 \langle P_k \rangle_t \right], \tag{3.21}$$

where $\langle T \rangle_t$ is the turbulent time scale

$$\langle T \rangle_t = max \left(\frac{\langle k \rangle_t}{\langle \epsilon \rangle_t}, 6 \sqrt{\frac{\nu}{\langle \epsilon \rangle_t}} \right), \tag{3.22}$$

$\langle L \rangle_t$ is the turbulent length scale

$$\langle L \rangle_t = C_L max \left[\frac{\langle k \rangle_t^{\frac{3}{2}}}{\langle \epsilon \rangle_t}, C_\eta \frac{\nu^3}{\langle \epsilon \rangle_t}^{\frac{1}{4}} \right], \tag{3.23}$$

and $\langle \alpha \rangle_t$ is defined as

$$\langle \alpha \rangle_t = \frac{1}{\langle T \rangle_t} \left[(C_1 - 6) \langle v^2 \rangle_t - \frac{2}{3} \langle k \rangle_t (C_1 - 1) \right]. \tag{3.24}$$

The eddy viscosity $\langle \nu_T \rangle_t$ is given by

$$\langle \nu_T \rangle_t = C_\mu \left\langle v^2 \right\rangle_t \langle T \rangle_t \,. \tag{3.25}$$

The model coefficients are reported in Table [3.2] and the boundary conditions to be imposed at the wall are: $\langle k \rangle_t = 0$, $\nabla \langle \epsilon \rangle_t = 0$, $\langle v^2 \rangle_t$ and $\langle f \rangle_t = 0$.

C_μ	C_1	C_2	C_L	C_η	$\langle C_{\epsilon 1} \rangle_t$	$C_{\epsilon 2}$	σ_k	σ_ϵ
0.22	1.4	0.3	0.23	70	$1.4\left[1 + 0.05\ min\left(\sqrt{\frac{\langle k \rangle_t}{\langle v^2 \rangle_t}}, 100\right)\right]$	1.9	1	1.3

Table 3.2: $\overline{v^2} - f$ *model: Constants and Functions*

Chapter 4

The plane channel flow and OpenFOAM

4.1 Averaging operators

The relevant operators used in this work are here introduced. Given a quantity $a(x)$, it is averaged along the x-direction as:

$$\langle a \rangle_x = \frac{1}{L_x} \int_0^{L_x} a(x)\, dx; \tag{4.1}$$

a quantity $a(z)$ is averaged along the z-direction as:

$$\langle a \rangle_z = \frac{1}{L_z} \int_0^{L_z} a(z)\, dz; \tag{4.2}$$

a quantity $a(t)$ is averaged along the time t as:

$$\langle a \rangle_t = \frac{1}{T} \int_0^{T} a(t)\, dx; \tag{4.3}$$

and, analogously to previous work [35], a quantity $a(y)$ is integrated along the y-direction as:

$$\langle a \rangle_y = \int_0^{h} a(y)\, dy. \tag{4.4}$$

Given a quantity $a(x, y, z, t)$, averaged over the N wavelengths λ_x as:

$$a(x, y, z, t) = \frac{1}{N} \sum_{n=0}^{N-1} a(n\lambda_x + x, y, z, t), \tag{4.5}$$

it is convenient to define the following operators:

$$\langle a \rangle_{zt}(xy) = \frac{1}{L_z}\frac{1}{T}\frac{1}{N}\int_0^T\int_0^{L_z}\sum_{n=0}^{N-1} a(n\lambda_x + x, y, z, t)\,dz\,dt, \tag{4.6}$$

$$\langle a \rangle_{xzt}(y) = \frac{1}{\lambda_x}\frac{1}{L_z}\frac{1}{T}\frac{1}{N}\int_0^T\int_0^{L_z}\int_0^{\lambda_x}\sum_{n=0}^{N-1} a(n\lambda_x + x, y, z, t)\,dx\,dz\,dt, \tag{4.7}$$

$$\langle a \rangle_{xy}(zt) = \frac{1}{\lambda_x}\frac{1}{N}\int_0^h\int_0^{\lambda_x}\sum_{n=0}^{N-1} a(n\lambda_x + x, y, z, t)\,dx\,dy. \tag{4.8}$$

$$[a] = \langle a \rangle_{xyzt} = \frac{1}{\lambda_x}\frac{1}{L_z}\frac{1}{T}\frac{1}{N}\int_0^T\int_0^{L_z}\int_0^h\int_0^{\lambda_x}\sum_{n=0}^{N-1} a(n\lambda_x + x, y, z, t)\,dx\,dy\,dz\,dt. \tag{4.9}$$

4.2 Flow configuration

We consider an incompressible fully developed turbulent flow between two parallel flat plates, assumed infinitely long and wide, at a distance of $2h$. Geometry and coordinate system are shown in Fig. [1.1]. The flow is statistically stationary and symmetric about mid-plane $y = h$. The mean flow is in the streamwise x direction, it is driven by a streamwise pressure gradient, calculated every time step in order to guarantee a constant flow rate. The *bulk velocity* U_b is defined as

$$U_b = \frac{[U]}{h}. \tag{4.10}$$

In the reference case (x,z) are both homogeneous directions, whereas when the steady forcing

$$W = A\sin\left(\frac{2\pi}{\lambda_x}x\right) \tag{4.11}$$

is applied the x-direction is not a homogeneous direction anymore. The forcing parameters are chosen to facilitate comparison of the results with those already available by DNS studies, thus a constant forcing amplitude $A^+ = 12$ and a constant wavelength $\lambda_x^+ = 1250$ are considered in this study.

Re_τ	L_x/h	L_x^+	N_x x N_y
200	6.25	1250	20 x 100
1000	6.25	1250	100 x 500

Table 4.1: Computational domain size and spatial resolution for two sets of simulations carried out at different values of the friction Reynolds number Re_τ

The computational domain size is reported in Table [4.1]: in particular the streamwise length of the computational domain coincides with the wavelength λ_x^+, eliminating all the quantities derived over x when they are averaged in this direction.

The relevant equations of motion for the mean flow are the continuity equation:

$$\frac{\partial \langle U \rangle_{zt}}{\partial x} + \frac{\partial \langle V \rangle_{zt}}{\partial y} = 0 \tag{4.12}$$

and the mean-momentum equations:

$$\begin{gathered}\underbrace{\frac{\partial(\langle U \rangle_{zt} \langle U \rangle_{zt})}{\partial x}}_{A_x} + \underbrace{\frac{\partial(\langle V \rangle_{zt} \langle U \rangle_{zt})}{\partial y}}_{B_x} = -\underbrace{\frac{1}{\rho}\frac{\partial \langle p \rangle_{zt}}{\partial x}}_{C_x} \\ + \underbrace{\nu\frac{\partial^2 \langle U \rangle_{zt}}{\partial x^2}}_{D_x} + \underbrace{\nu\frac{\partial^2 \langle U \rangle_{zt}}{\partial y^2}}_{E_x} - \underbrace{\frac{\partial \langle uu \rangle_{zt}}{\partial x}}_{F_x} - \underbrace{\frac{\partial \langle uv \rangle_{zt}}{\partial y}}_{G_x};\end{gathered} \tag{4.13}$$

$$\begin{gathered}\underbrace{\frac{\partial(\langle U \rangle_{zt} \langle V \rangle_{zt})}{\partial x}}_{A_y} + \underbrace{\frac{\partial(\langle V \rangle_{zt} \langle V \rangle_{zt})}{\partial y}}_{B_y} = -\underbrace{\frac{1}{\rho}\frac{\partial \langle p \rangle_{zt}}{\partial y}}_{C_y} \\ + \underbrace{\nu\frac{\partial^2 \langle V \rangle_{zt}}{\partial x^2}}_{D_y} + \underbrace{\nu\frac{\partial^2 \langle V \rangle_{zt}}{\partial y^2}}_{E_y} - \underbrace{\frac{\partial \langle uv \rangle_{zt}}{\partial x}}_{F_y} - \underbrace{\frac{\partial \langle vv \rangle_{zt}}{\partial y}}_{G_y};\end{gathered} \tag{4.14}$$

$$\begin{aligned}\underbrace{\frac{\partial(\langle U\rangle_{zt}\langle W\rangle_{zt})}{\partial x}}_{A_z}+\underbrace{\frac{\partial(\langle V\rangle_{zt}\langle W\rangle_{zt})}{\partial y}}_{B_z}&=-\underbrace{\frac{1}{\rho}\frac{\partial\langle p\rangle_{zt}}{\partial z}}_{C_z}\\&+\underbrace{\nu\frac{\partial^2\langle W\rangle_{zt}}{\partial x^2}}_{D_z}+\underbrace{\nu\frac{\partial^2\langle W\rangle_{zt}}{\partial y^2}}_{E_z}-\underbrace{\frac{\partial\langle uw\rangle_{zt}}{\partial x}}_{F_z}-\underbrace{\frac{\partial\langle vw\rangle_{zt}}{\partial y}}_{G_z}.\end{aligned}\tag{4.15}$$

where the terms that only arise when the forcing (4.11) is applied are highlighted in red.

Studying the axial and the wall-normal mean equations, emerges that after averaging over x terms A_x, A_y, D_x, D_y, F_x and F_y are null because the spatial periodicity imposes that $\langle U\rangle_{zt}\langle U\rangle_{zt}|_{x=L_x}$, $\nu\frac{\partial\langle U\rangle_{zt}}{\partial x}\Big|_{x=L_x}$, $\langle uu\rangle_{zt}|_{x=L_x}$ is equal respectively to $\langle U\rangle_{zt}\langle U\rangle_{zt}|_{x=}$, $\nu\frac{\partial\langle U\rangle_{zt}}{\partial x}\Big|_{x=0}$, $\langle uu\rangle_{zt}|_{x=0}$, and $\langle U\rangle_{zt}\langle V\rangle_{zt}|_{x=L_x}$, $\nu\frac{\partial\langle V\rangle_{zt}}{\partial x}\Big|_{x=L_x}$, $\langle uv\rangle_{zt}|_{x=L_x}$ is equally respectively to $\langle U\rangle_{zt}\langle V\rangle_{zt}|_{x=0}$, $\nu\frac{\partial\langle V\rangle_{zt}}{\partial x}\Big|_{x=0}$, $\langle uv\rangle_{zt}|_{x=0}$.

The equations become:

$$\left\langle\langle V\rangle_{zt}\frac{\partial\langle U\rangle_{zt}}{\partial y}\right\rangle_x=-\left\langle\frac{1}{\rho}\frac{\partial\langle p\rangle_{zt}}{\partial x}\right\rangle_x+\left\langle\nu\frac{\partial^2\langle U\rangle_{zt}}{\partial y^2}\right\rangle_x-\left\langle\frac{\partial\langle uv\rangle_{zt}}{\partial y}\right\rangle_x\tag{4.16}$$

$$\left\langle\langle V\rangle_{zt}\frac{\partial\langle V\rangle_{zt}}{\partial y}\right\rangle_x=-\left\langle\frac{1}{\rho}\frac{\partial\langle p\rangle_{zt}}{\partial y}\right\rangle_x+\left\langle\nu\frac{\partial^2\langle V\rangle_{zt}}{\partial y^2}\right\rangle_x-\left\langle\frac{\partial\langle vv\rangle_{zt}}{\partial y}\right\rangle_x.\tag{4.17}$$

Since some terms are empirically found to be negligible[1], the equations reduce to their counterpart for the uncontrolled flow:

$$\left\langle\frac{1}{\rho}\frac{\partial\langle p\rangle_{zt}}{\partial x}\right\rangle_x-\left\langle\nu\frac{\partial^2\langle U\rangle_{zt}}{\partial y^2}\right\rangle_x+\left\langle\frac{\partial\langle uv\rangle_{zt}}{\partial y}\right\rangle_x=0\tag{4.18}$$

$$\left\langle\frac{1}{\rho}\frac{\partial\langle p\rangle_{zt}}{\partial y}\right\rangle_x+\left\langle\frac{\partial\langle vv\rangle_{zt}}{\partial y}\right\rangle_x=0.\tag{4.19}$$

Observing that $\left\langle\frac{\partial\langle vv\rangle_{zt}}{\partial x}\right\rangle_x=0$, the latter leads to:

$$\left\langle\frac{\partial\langle p\rangle_{zt}}{\partial x}\right\rangle_x=\left\langle\frac{d\langle p_w\rangle_{zt}}{dx}\right\rangle_x\tag{4.20}$$

---

[1] $\left\langle\langle V\rangle_{zt}\frac{\partial\langle U\rangle_{zt}}{\partial y}\right\rangle_x\simeq10^{-6}$; $\left\langle\langle V\rangle_{zt}\frac{\partial\langle V\rangle_{zt}}{\partial y}\right\rangle_x\simeq10^{-8}$; $\left\langle\nu\frac{\partial^2\langle V\rangle_{zt}}{\partial y^2}\right\rangle_x\simeq10^{-7}$

where $\langle p_w \rangle_{zt} = \langle p(x,0,0) \rangle_{zt}$ is the mean pressure on the wall. The axial mean-momentum equation leads to:

$$-\left\langle \frac{d \langle p_w \rangle_{zt}}{dx} \right\rangle_x = \frac{\langle \tau_w \rangle_{xzt}}{h}, \tag{4.21}$$

where $\langle \tau_w \rangle_{xzt}$ is the x-component of the averaged wall shear stress defined as:

$$\langle \tau_w \rangle_{xzt} = \rho\nu \left\langle \frac{d \langle U \rangle_{zt}}{dy} \right\rangle_x \bigg|_{y=0}. \tag{4.22}$$

The viscous stress is relevant only near the wall, therefore the appropriate velocity scale in this region is the friction velocity:

$$u_\tau = \sqrt{\frac{\langle \tau_w \rangle_{xzt}}{\rho}} \tag{4.23}$$

The friction Reynolds number is defined as:

$$Re_\tau = \frac{u_\tau h}{\nu}. \tag{4.24}$$

The skin friction coefficient is:

$$\langle C_f \rangle_{xzt} = \frac{\langle \tau_w \rangle_{xzt}}{\frac{1}{2}\rho U_b^2}. \tag{4.25}$$

This can be obtained, for the uncontrolled flow, by means of Dean's correlation:

$$\langle C_f \rangle_{xzt} = 0.073 Re^{-0.25} \tag{4.26}$$

if the Reynolds number is sufficiently high, otherwise a more correct valuation of the $\langle C_f \rangle_{xzt}$ is achievable by DNS studies.

4.3 Numerical solution

The solution of the RANS equations is performed using the open source software OpenFOAM (Open Field Operation and Manipulation). It is a numerical simulation software package with large CFD and multi-physics capabilities, widely employed by commercial and academic organisations.

OpenFOAM is a C++ library, used to develop the applications, that are solvers and utilities. The users are free to customise new applications, although various of them are included in the OpenFOAM distribution. The solver uses the finite volume method for the discretization of the governing flow equations over all the control volume of the solution domain. The unknown flow variables are substituted by finite-difference-type approximations. This converts the integral equations in a system of algebraic equations, solved by an iterative method. The solver used in this work is *simpleFoam*: a steady-state solver for incompressible, turbulent flow.

4.3.1 Generation of the Mesh

The mesh is generated by means of the utilitiy *blockMesh*: a dictionary file named *blockMeshDict* located in the *constant/polyMesh* directory that generates the mesh and writes out the mesh data to points, faces, cells and boundary files in the same directory.

A typical structure of the *blockMeshDict* includes different kewywords. The most important are:

- **convertToMeters**: scaling factor for the vertex coordinates.
- **Vertices**: a list of the vertex coordinates of the computational domain.

```
vertices
(
    (0 0 0)                    //vertex number 0
    (0.6147 0 0)               //vertex number 1
    (0 0.09825 0)              //vertex number 2
    ...
)
);
```

- **Blocks**: a list of vertex labels, a vector giving the number of cells required in each direction and the type and list of cell expansion ratio in each direction.

```
blocks
(
    hex (0 1 3 2 4 5 7 6)    // vertex numbers
    (20 100 1)               // numbers of cells
    simpleGrading (1 4 1)    // cell expansion ratios
);
```

The mesh consists of blocks of hexaedral cells, whose size is constant in the two directions (x,z). In the cross-stream direction y, a grading (i.e a uniform expansion in a specified direction) is required in order to guarantee a fitting resolution in the near wall area: since no wall function are used, y^+ has to be approximately 1 and at least the first five cells have to lie below $y^+ = 10$ to assure that the SSL is adequately evaluated.

- **Boundary**: a list of surfaces corresponding to the boundary of the physical domain, where boundary conditions have to be specified. The *cyclic* boundary conditions are used in the directions (x,z) in order to practically implement the infinite computational domain. They require the specification of the name of the related cyclic patch through the *neighbourPatch* keyword.

```
boundary
(
    bottomWall
    {
        type            wall;
        faces           (0 1 5 4);
    }
    topWall
    {
        type            symmetryPlane;
        faces           (2 6 7 3);
    }

    inflow
    {
        type            cyclic;
        neighbourPatch  outflow;
        faces           (1 3 7 5);
    }
    outflow
    {
        type            cyclic;
        neighbourPatch  inflow;
        faces           (0 4 6 2);
    }

    ...
);
```

The *symmetryPlane* boundary condition, imposed on the patch *topWall*, allows the study only of half of the channel, halving the computational cost. In order to perform a 2D simulation only one cell in the z direction is used.

4.3.2 Boundary conditions

The initial fields data are stored in the *0* subdirectory of the case directory.

Since both *cyclic* and *symmetryPlane* boundary conditions are physical conditions, they do not require any values to be imposed, thus the *wall* boundary conditions are the only crucial ones. In fact the *cyclic* boundary conditions, also know as periodic boundary conditions, treat two boundary regions as if they are physically connected, imposing that for each variable the value at the nodes of the patch is equal to the value at the nodes of its neighbour patch, while the *symmetryPlane* boundary condition implies that the components of the velocity and of the gradient normal to the boundary should be fixed zero.

At the wall the numerical boundary conditions of Dirichelet and Neumann are used respectively for velocity and for pressure. The forcing (4.11) is applied by means of the boundary condition on the velocity at the wall: a new library of OpenFOAM, addressed in the next section is used in order to obtain sinusoidal boundary conditions. In Chapter (3) the boundary conditions related to the turbulent variables have been discussed. In particular the dissipation rate ϵ must be zero at the wall in the Launder Sharma $k-\epsilon$ model and *zeroGradient* in the $\overline{v^2}-f$ model. The latter requires two additional fields f:

```
FoamFile
{
    version     2.0;
    format      ascii;
    class       volScalarField;
    object      f;
}
// * * * ** * * * * * * * * * * * * * * * * * * * * * //

dimensions      [ 0 0 -1 0 0 0 0 ];

internalField   uniform 0.07;

boundaryField
{
   bottomWall
    {
       type            fixedValue;
       value           uniform 0;
    }
```

and v^2:

```
FoamFile
{
    version     2.0;
    format      ascii;
    class       volScalarField;
    object      v2;
}
// * * * ** * * * * * * * * * * * * * * * * * * * * * //

dimensions      [ 0 2 -2 0 0 0 0 ];
```

```
internalField   uniform 4.12e-5;

boundaryField
{
   bottomWall
    {
        type            fixedValue;
        value           uniform 1e-20;
    }
```

corresponding respectively to the two additional equations solved (i.e. Eq.(3.20) and Eq. (3.21)).

swak4foam

Stands for SWiss Army Knife for Foam. It is a library that offers a large number of utilities, such as *groovyBC* to specify arbitrary boundary conditions based on expressions. It is used in this work in order to impose the sinusoidal forcing (4.11) at the wall:

```
boundaryField
{
    bottomWall
    {
        type             groovyBC;
        value            uniform (0 0 1);
        variables        "A=0.336;xp=pos().x;lambdaX=0.6147;";
        valueExpression  "vector (0, 0, A*sin(xp*(2*pi)/lambdaX))";
    }
...
}
```

The following libraries need to be added in the dictionary file *controlDict* located in the *system* directory:

```
libs
(
    "libsimpleSwakFunctionObjects.so"
    "libswakFunctionObjects.so"
    "libgroovyBC.so"
    ...
);
```

4.3.3 Residuals

The convergence of the iterative solution is evaluated by means of the residuals. The discretization of the Navier–Stokes equations through the finite volume method over all the control volume of the solution domain, leads to an algebraical linear system:

$$A\mathbf{x} = \mathbf{b}, \tag{4.27}$$

where A is a matrix of order n, $\mathbf{x}$ is the vector of the solution at a specific cell and at a determined time-step and $\mathbf{b} \in \Re^n$. The residuals are calculated as

$$\mathbf{R} = A\mathbf{x} - \mathbf{b}. \tag{4.28}$$

In OpenFOAM a normalization of the residuals is made by means of the definition of normalization factor F:

$$F = \sum(\|\mathbf{w_A} - \mathbf{p_A}\| + \|b - \mathbf{p_A}\|) + 10^{20}, \tag{4.29}$$

where $\mathbf{w_A} = A\mathbf{x}$ and $\mathbf{p_A} = A \langle \mathbf{x} \rangle_{xyzt}$. The normalised residuals are:

$$r = \frac{\sum \|\mathbf{b} - \mathbf{w_A}\|}{F}. \tag{4.30}$$

The error committed using the approximated solution $\mathbf{x}$ in place of the exact solution $\mathbf{x_e}$ depends on the normalized residuals r, therefore a reduction of them involves a reduction of the error.

Chapter 5

Results

Given the fundamental role played by the the skin friction coefficient $\langle C_f \rangle_{xzt}$ in the assessment of the drag reduction performance, as follows from Eq. (2.2), its value achieved via RANS is here discussed both in the reference and in the forced case at different values of the Reynolds number. A quantitative analysis of the results calculated is made, starting from the DNS data. The of energy balance for the mean and turbulent kinetic energy is studied in order to investigate the mechanism of the drag reduction prediction.

The percentage error made by the RANS simulations, for a quantity a, is calculated as:

$$\Delta a = \frac{\langle a \rangle - a_{DNS}}{a_{DNS}} \tag{5.1}$$

where $\langle a \rangle$ is the calculated value after suitable average and a_{DNS} is the computed via DNS one.

5.1 DNS

In order to make a quantitative analysis possible, the relevant quantities are calculated by means of a parallel DNS solver [26], based on mixed discretization:Fourier expansion in the homogeneous directions and compact fourth-order accurate explicit compact finite difference schemes in the wall-normal direction. The computational domain has dimensions of $L_x^* = 6\pi h$, $L_y^* = 2h$ and $L_z^* = 3\pi h$ in the three directions. The employed number of modes/points is given by $N_x = 320$, $N_y = 160$ and $N_z = 320$.

The field of the spanwise velocity component achieved when the forcing (4.11) is applied, is shown in Fig. [5.1].

5.1.1 Skin Friction Coefficient

The skin friction coefficients are already know from previous DNS studies, thus are not calculated in the present work. In the reference case, the value of the skin friction coefficient is found to be $C_{f,0_{DNS}} = 0.00793$ when $Re_\tau = 200$, as reported in the DNS study of Quadrio and Ricco [32], and $C_{f,0_{DNS}} = 0.00517$ when $Re_\tau = 1000$ as computed by means of Dean's correlation (4.26) or starting from the DNS data of Hoyas *et al.* [18]. In the forced case, a manipulation of Eq. (2.2) leads to:

$$C_{f_{DNS}} = C_{f,0_{DNS}}(1 - R_{DNS}), \tag{5.2}$$

where, since $C_{f,0_{DNS}}$ and R_{DNS} are known (see (2.6)), the values of $C_{f_{DNS}} = 0.00436$ and $C_{f_{DNS}} = 0.00362$ are found, respectively at $Re_\tau = 200$ and $Re_\tau = 1000$.

5.1.2 Mechanism of drag reduction

With the aim of understanding the mechanism of the drag reduction prediction by means of the turbulence model, the energy balance for the mean and fluctuating flow fields is studied. The two equations for mean and kinetic energy are then summed together to obtain the global balance for the total kinetic energy. The terms in red are those arising only when the forcing is applied. Since a constant mass flow rate is imposed in the simulation, the reduction of the skin friction coefficient $\langle C_f \rangle_{xzt}$ is attributed to a decrease of $\langle \tau_w \rangle_{xzt}$.

Balance equation for the MKE

The transport equation for MKE $\langle K \rangle_{zt} = \frac{1}{2}\left(\langle U \rangle_{zt}^2 + \langle V \rangle_{zt}^2 + \langle W \rangle_{zt}^2\right)$ is:

$$\underbrace{\langle U \rangle_{zt} \frac{\partial \langle K \rangle_{zt}}{\partial x}}_{1} + \underbrace{\langle V \rangle_{zt} \frac{\partial \langle K \rangle_{zt}}{\partial y}}_{2} + \underbrace{\frac{\partial \langle T_x \rangle_{zt}}{\partial x}}_{3} + \underbrace{\frac{\partial \langle T_y \rangle_{zt}}{\partial y}}_{4} = -\underbrace{\langle P_k \rangle_{zt}}_{5} - \underbrace{\langle \mathscr{E} \rangle_{zt}}_{6} \tag{5.3}$$

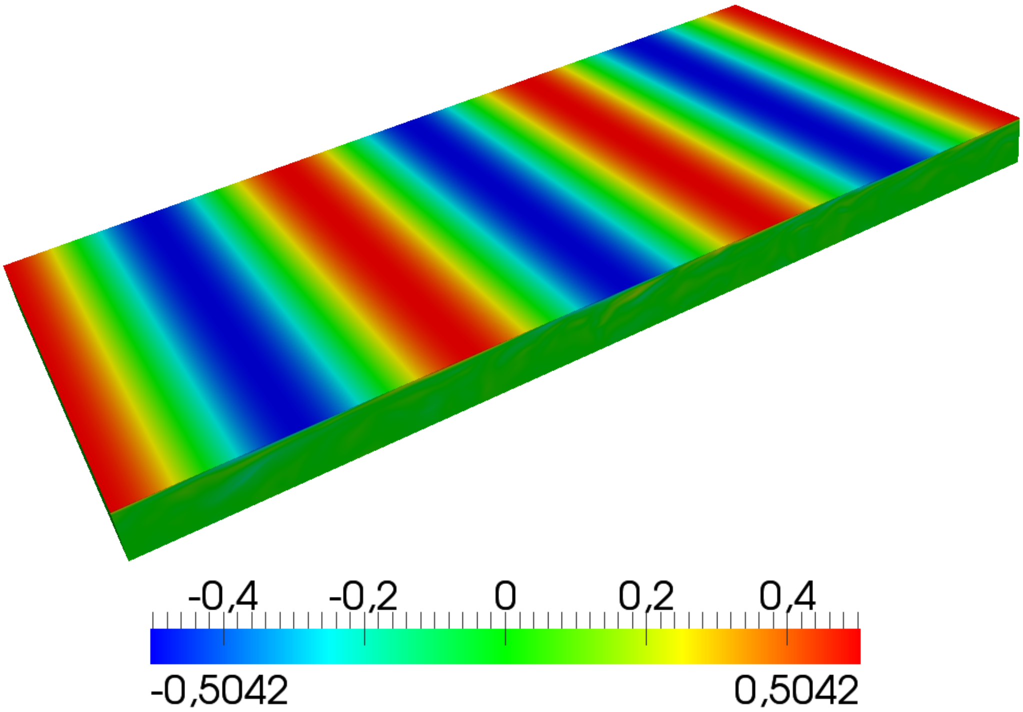

Figure 5.1: Field of the spanwise velocity component W calculated via DNS

where

$$\begin{aligned}\langle T_x\rangle_{zt} &= \langle U\rangle_{zt}\langle uu\rangle_{zt} + \langle V\rangle_{zt}\langle uv\rangle_{zt} + \langle W\rangle_{zt}\langle uw\rangle_{zt} + \langle U\rangle_{zt}\frac{\langle P\rangle_{zt}}{\rho} \\ &-2\nu\langle U\rangle_{zt}\frac{\partial\langle U\rangle_{zt}}{\partial x} - \nu\langle V\rangle_{zt}\left(\frac{\partial\langle U\rangle_{zt}}{\partial y} + \frac{\partial\langle V\rangle_{zt}}{\partial x}\right) - \nu\langle W\rangle_{zt}\frac{\partial\langle W\rangle_{zt}}{\partial x},\end{aligned} \tag{5.4}$$

$$\begin{aligned}\langle T_y\rangle_{zt} = \langle U\rangle_{zt}\langle uv\rangle_{zt} + \langle V\rangle_{zt}\langle vv\rangle_{zt} + \langle W\rangle_{zt}\langle vw\rangle_{zt} + \langle V\rangle_{zt}\frac{\langle P\rangle_{zt}}{\rho} \\ -\nu\langle U\rangle_{zt}\frac{\partial\langle U\rangle_{zt}}{\partial y} - \nu\langle U\rangle_{zt}\frac{\partial\langle V\rangle_{zt}}{\partial x} - 2\nu\langle V\rangle_{zt}\frac{\partial\langle V\rangle_{zt}}{\partial y} \\ -\nu\langle W\rangle_{zt}\frac{\partial\langle W\rangle_{zt}}{\partial y},\end{aligned} \tag{5.5}$$

$$\begin{aligned}\langle P_k\rangle_{zt} = &-\langle uu\rangle_{zt}\frac{\partial\langle U\rangle_{zt}}{\partial x} - \langle uv\rangle_{zt}\frac{\partial\langle U\rangle_{zt}}{\partial y} - \langle uv\rangle_{zt}\frac{\partial\langle V\rangle_{zt}}{\partial x} \\ &-\langle vv\rangle_{zt}\frac{\partial\langle V\rangle_{zt}}{\partial y} - \langle uw\rangle_{zt}\frac{\partial\langle W\rangle_{zt}}{\partial x} - \langle vw\rangle_{zt}\frac{\partial\langle W\rangle_{zt}}{\partial y},\end{aligned} \tag{5.6}$$

$$\begin{aligned}\langle \mathscr{E} \rangle_{zt} = 2\nu \left(\frac{\partial \langle U \rangle_{zt}}{\partial x} \right)^2 + 2\nu \left(\frac{\partial \langle V \rangle_{zt}}{\partial y} \right)^2 + 2\nu \frac{\partial \langle U \rangle_{zt}}{\partial y} \frac{\partial \langle V \rangle_{zt}}{\partial x} + \nu \left(\frac{\partial \langle U \rangle_{zt}}{\partial y} \right)^2 \\ + \nu \left(\frac{\partial \langle V \rangle_{zt}}{\partial x} \right)^2 + \nu \left(\frac{\partial \langle W \rangle_{zt}}{\partial x} \right)^2 + \nu \left(\frac{\partial \langle W \rangle_{zt}}{\partial y} \right)^2 .\end{aligned} \tag{5.7}$$

The convection of MKE is expressed by terms 1 and 2, while term 3, as well as term 4, consists of the sum of the transport work performed by the Reynolds stresses, the pressure work and the transport work done by the mean viscous stresses. Term 5 is the work of deformation carried out by the Reynolds stresses through which energy is exchanged between the mean flow and the fluctuating flow and term 6 is the mean flow viscous dissipation. In order to make $\langle \tau_w \rangle_{xzt}$ appear in the energy balance, the MKE is space averaged along the x-direction and integrated along y. Once averaged along x term 3 becomes null, except for the power used to drive the flow along x that is:

$$\left\langle \frac{\partial}{\partial x} \left[\langle U \rangle_{zt} \frac{\langle P \rangle_{zt}}{\rho} \right] \right\rangle_x = \left\langle \frac{\partial \langle U \rangle_{zt}}{\partial x} \frac{\langle P \rangle_{zt}}{\rho} \right\rangle_x - \left\langle \frac{\langle U \rangle_{zt}}{\rho} \frac{\partial \langle P \rangle_{zt}}{\partial x} \right\rangle_x . \tag{5.8}$$

where the first term is negligible being its maximum$\simeq -10^{-8}$. The second term can be rewritten observing that:

$$\langle U \rangle_{zt} (x, y) = \langle \langle U \rangle_{zt} \rangle_x (y) + \widehat{\langle U \rangle_{zt}} (x, y). \tag{5.9}$$

This leads, by means of (4.21), to:

$$\begin{aligned}\left\langle \frac{\langle U \rangle_{zt}}{\rho} \frac{\partial \langle P \rangle_{zt}}{\partial x} \right\rangle_x &= \left\langle \left[\langle \langle U \rangle_{zt} \rangle_x (y) + \widehat{\langle U \rangle_{zt}} (x, y) \right] \frac{\partial P}{\partial x} \right\rangle_x \\ &= - \frac{\langle \langle U \rangle_{zt} \rangle_x}{\rho} \frac{\langle \tau_w \rangle_{xzt}}{h}\end{aligned} \tag{5.10}$$

because $\left\langle \widehat{\langle U \rangle_{zt}} \right\rangle_x$ is null. Upon y-integration the terms $\left\langle \left\langle \frac{\partial}{\partial y} \left[\langle U \rangle_{zt} \langle uv \rangle_{zt} \right] \right\rangle_x \right\rangle_y$, $\left\langle \left\langle \frac{\partial}{\partial y} \left[\langle V \rangle_{zt} \langle vv \rangle_{zt} \right] \right\rangle_x \right\rangle_y$ and $\left\langle \left\langle \frac{\partial}{\partial y} \left[\langle W \rangle_{zt} \langle vw \rangle_{zt} \right] \right\rangle_x \right\rangle_y$ become null because of the Reynolds stresses $\langle uv \rangle_{zt} = 0$, $\langle vv \rangle_{zt} = 0$ and $\langle vw \rangle_{zt} = 0$ both at y=0, where no slip condition are imposed for the velocity, and at y=h for symmetry. The terms $\left\langle \left\langle \frac{\partial}{\partial y} \left[\nu \langle U \rangle_{zt} \frac{\partial \langle U \rangle_{zt}}{\partial y} \right] \right\rangle_x \right\rangle_y$ and $\left\langle \left\langle \frac{\partial}{\partial y} \left[\nu \langle V \rangle_{zt} \frac{\partial \langle V \rangle_{zt}}{\partial y} \right] \right\rangle_x \right\rangle_y$ are also null because $\langle U \rangle_{zt} = 0$ and $\langle V \rangle_{zt} = 0$ at y=0 and $\frac{\partial \langle U \rangle_{zt}}{\partial y} = 0$ and

$\frac{\partial \langle V\rangle_{zt}}{\partial y} = 0$ at y=h.

The global transport equation for MKE is:

$$\begin{aligned}
&\left\langle \langle U\rangle_{zt} \frac{\partial \langle K\rangle_{zt}}{\partial x} \right\rangle_{xy} + \left\langle \langle V\rangle_{zt} \frac{\partial \langle K\rangle_{zt}}{\partial y} \right\rangle_{xy} + \left\langle \frac{\partial \langle U\rangle_{zt}}{\partial x} \frac{\langle p\rangle_{zt}}{\rho} \right\rangle_{xy} \\
&-U_b \frac{\langle \tau_w\rangle_{xzt}}{\rho} + \left\langle \frac{\partial}{\partial y} \left[\langle V\rangle_{zt} \frac{\langle P\rangle_{zt}}{\rho} \right] \right\rangle_{xy} - \left\langle \frac{\partial}{\partial y} \left[\nu \langle U\rangle_{zt} \frac{\partial \langle V\rangle_{zt}}{\partial x} \right] \right\rangle_{xy} \\
&- \left\langle \frac{\partial}{\partial y} \left[\nu \langle W\rangle_{zt} \frac{\partial \langle W\rangle_{zt}}{\partial y} \right] \right\rangle_{xy} = -\langle P_k\rangle_{xyzt} - \langle \mathscr{E}\rangle_{xyzt}
\end{aligned} \tag{5.11}$$

where

$$\begin{aligned}
\langle P_k\rangle_{xyzt} = &- \left\langle \langle uu\rangle_{zt} \frac{\partial \langle U\rangle_{zt}}{\partial x} \right\rangle_{xy} - \left\langle \langle uv\rangle_{zt} \frac{\partial \langle U\rangle_{zt}}{\partial y} \right\rangle_{xy} \\
&- \left\langle \langle uv\rangle_{zt} \frac{\partial \langle V\rangle_{zt}}{\partial x} \right\rangle_{xy} - \left\langle \langle vv\rangle_{zt} \frac{\partial \langle V\rangle_{zt}}{\partial y} \right\rangle_{xy} \\
&- \left\langle \langle uw\rangle_{zt} \frac{\partial \langle W\rangle_{zt}}{\partial x} \right\rangle_{xy} - \left\langle \langle vw\rangle_{zt} \frac{\partial \langle W\rangle_{zt}}{\partial y} \right\rangle_{xy},
\end{aligned} \tag{5.12}$$

$$\begin{aligned}
\langle \bar{\epsilon}\rangle_{xyzt} = &\left\langle 2\nu \left(\frac{\partial \langle U\rangle_{zt}}{\partial x} \right)^2 \right\rangle_{xy} + \left\langle 2\nu \left(\frac{\partial \langle V\rangle_{zt}}{\partial y} \right)^2 \right\rangle_{xy} \\
&+ \left\langle 2\nu \frac{\partial \langle U\rangle_{zt}}{\partial y} \frac{\partial \langle V\rangle_{zt}}{\partial x} \right\rangle_{xy} + \left\langle \nu \left(\frac{\partial \langle U\rangle_{zt}}{\partial y} \right)^2 \right\rangle_{xy} \\
&+ \left\langle \nu \left(\frac{\partial \langle V\rangle_{zt}}{\partial x} \right)^2 \right\rangle_{xy} + \left\langle \nu \left(\frac{\partial \langle W\rangle_{zt}}{\partial x} \right)^2 \right\rangle_{xy} \\
&+ \left\langle \nu \left(\frac{\partial \langle W\rangle_{zt}}{\partial y} \right)^2 \right\rangle_{xy}.
\end{aligned} \tag{5.13}$$

Since some terms are empirically found to be negligible[1] the equation reduces to:

---

[1] $\left\langle \langle U\rangle_{zt} \frac{\partial \langle K\rangle_{zt}}{\partial x} \right\rangle_{xy} \simeq 10^{-6}$; $\left\langle \langle V\rangle_{zt} \frac{\partial \langle K\rangle_{zt}}{\partial y} \right\rangle_{xy} \simeq -10^{-6}$; $\left\langle \frac{\partial}{\partial y} \left[\langle V\rangle_{zt} \frac{\langle P\rangle_{zt}}{\rho} \right] \right\rangle_{xy} \simeq 10^{-14}$; $\left\langle \frac{\partial}{\partial y} \left[\nu \langle U\rangle_{zt} \frac{\partial \langle V\rangle_{zt}}{\partial x} \right] \right\rangle_{xy} \simeq 10^{-6}$; $\left\langle \langle uu\rangle_{zt} \frac{\partial \langle U\rangle_{zt}}{\partial x} \right\rangle_{xy} \simeq 10^{-8}$; $\left\langle \langle uv\rangle_{zt} \frac{\partial \langle V\rangle_{zt}}{\partial x} \right\rangle_{xy} \simeq 10^{-5}$; $\left\langle \langle vv\rangle_{zt} \frac{\partial \langle V\rangle_{zt}}{\partial y} \right\rangle_{xy} \simeq -10^{-8}$; $\left\langle \langle uw\rangle_{zt} \frac{\partial \langle W\rangle_{zt}}{\partial x} \right\rangle_{xy} \simeq 10^{-7}$; $\left\langle 2\nu \left(\frac{\partial \langle U\rangle_{zt}}{\partial x} \right)^2 \right\rangle_{xy} \simeq 10^{-10}$; $\left\langle 2\nu \left(\frac{\partial \langle V\rangle_{zt}}{\partial y} \right)^2 \right\rangle_{xy} \simeq 10^{-10}$; $\left\langle 2\nu \frac{\partial \langle U\rangle_{zt}}{\partial y} \frac{\partial \langle V\rangle_{zt}}{\partial x} \right\rangle_{xy} \simeq 10^{-10}$; $\left\langle \nu \left(\frac{\partial \langle V\rangle_{zt}}{\partial x} \right)^2 \right\rangle_{xy} \simeq 10^{-12}$; $\left\langle \nu \left(\frac{\partial \langle W\rangle_{zt}}{\partial x} \right)^2 \right\rangle_{xy} \simeq 10^{-6}$.

$$\begin{aligned}\underbrace{-\frac{U_b}{\rho}\langle\tau_w\rangle_{xzt}}_{P} + \underbrace{\left\langle -\frac{\partial}{\partial y}\left(\nu\,\langle W\rangle_{zt}\,\frac{\partial\langle W\rangle_{zt}}{\partial y}\right)\right\rangle_{xy}}_{P_{in}} &= \underbrace{\left\langle \langle uv\rangle_{zt}\,\frac{\partial\langle U\rangle_{zt}}{\partial y}\right\rangle_{xy}}_{\mathscr{P}_{uv}} \\ + \underbrace{\left\langle \langle vw\rangle_{zt}\,\frac{\partial\langle W\rangle_{zt}}{\partial y}\right\rangle_{xy}}_{\mathscr{P}_{vw}} - \underbrace{\left\langle \nu\left(\frac{\partial\langle W\rangle_{zt}}{\partial y}\right)^2\right\rangle_{xy}}_{\mathscr{D}_W} &- \underbrace{\left\langle \nu\left(\frac{\partial\langle U\rangle_{zt}}{\partial y}\right)^2\right\rangle_{xy}}_{\mathscr{D}_U}\,.\end{aligned} \tag{5.14}$$

The terms on the left-hand side represent the energy inputs: the first term, where τ_w explicitly appears, denotes the global energy pumped into the system through the external pressure gradient whereas the second term is the energy spent to realise the forcing against the frictional resistance of the fluid. Terms $\mathscr{P}_{uv}$ and $\mathscr{P}_{vw}$ are sinks for MKE and production terms in the global TKE balance where they appear with opposite sign. The global viscous dissipation, due to the gradient of the mean streamwise and spanwise velocity components, corresponds to terms $\mathscr{D}_U$ and $\mathscr{D}_W$. The balance in (5.14) states that part of the energy inputs is transferred to the turbulence via $\mathscr{P}_{uv}$ and $\mathscr{P}_{vw}$ and the remaining part is dissipated into heat through $\mathscr{D}_U$ and $\mathscr{D}_W$.

Balance equation for the TKE

The transport equation for TKE reads:

$$\underbrace{\langle U\rangle_{zt}\frac{\partial\langle k\rangle_{zt}}{\partial x}}_{1} + \underbrace{\langle V\rangle_{zt}\frac{\partial\langle k\rangle_{zt}}{\partial y}}_{2} + \underbrace{\frac{\partial\langle t_x\rangle_{zt}}{\partial x}}_{3} + \underbrace{\frac{\partial\langle t_y\rangle_{zt}}{\partial y}}_{4} = \underbrace{\langle P_k\rangle_{zt}}_{5} - \underbrace{\langle \epsilon\rangle_{zt}}_{6} \tag{5.15}$$

where

$$\begin{aligned}\langle t_x\rangle_{zt} &= \frac{1}{2}\langle uuu\rangle_{zt} + \frac{1}{2}\langle uvv\rangle_{zt} + \frac{1}{2}\langle uww\rangle_{zt} + \frac{\langle up\rangle_{zt}}{\rho} \\ -2\nu\left\langle u\frac{\partial u}{\partial x}\right\rangle_{zt} &- \nu\left\langle v\left(\frac{\partial u}{\partial y}+\frac{\partial v}{\partial x}\right)\right\rangle_{zt} - \nu\left\langle w\left(\frac{\partial u}{\partial z}+\frac{\partial w}{\partial x}\right)\right\rangle_{zt}\,,\end{aligned} \tag{5.16}$$

$$\begin{aligned}\langle t_y\rangle_{zt} &= \frac{1}{2}\langle vuu\rangle_{zt} + \frac{1}{2}\langle vvv\rangle_{zt} + \frac{1}{2}\langle vww\rangle_{zt} + \frac{\langle vp\rangle_{zt}}{\rho} \\ -\nu\left\langle u\left(\frac{\partial v}{\partial x}+\frac{\partial u}{\partial y}\right)\right\rangle_{zt} &- 2\nu\left\langle v\frac{\partial v}{\partial y}\right\rangle_{zt} - \nu\left\langle w\left(\frac{\partial w}{\partial y}+\frac{\partial v}{\partial z}\right)\right\rangle_{zt}\,,\end{aligned} \tag{5.17}$$

and $\langle P_k\rangle_{zt}$ is the turbulent kinetic production (5.6). Terms 1 and 2 denote the convection of TKE, terms 3 and 4 the diffusion, term 5 is the production of TKE and also appears in MKE as sink. Term 6 is the viscous dissipation of TKE. Analogously to the analysis of the MKE equation, the averaging over x leads to $\left\langle \frac{\partial \langle t_x\rangle_{zt}}{\partial x}\right\rangle_x = 0$ for the spatial periodicity, whereas the integration along y eliminates $\left\langle \frac{1}{2}\frac{\partial\langle vuu\rangle_{zt}}{\partial y}\right\rangle_{xy}$, $\left\langle \frac{1}{2}\frac{\partial\langle vvv\rangle_{zt}}{\partial y}\right\rangle_{xy} + \left\langle \frac{1}{2}\frac{\partial\langle vww\rangle_{zt}}{\partial y}\right\rangle_{xy}$ and $\left\langle \frac{1}{\rho}\frac{\partial\langle vp\rangle_{zt}}{\partial y}\right\rangle_{xy}$ because $v = 0$ both at $y = h$ and $y = 0$, the term $\left\langle \frac{\partial}{\partial y}\left\langle \nu u\frac{\partial u}{\partial y}\right\rangle_{zt}\right\rangle_{xy}$ is null because $u = 0$ at $y = 0$ and $\frac{\partial u}{\partial y} = 0$ at $y = h$, $\left\langle \frac{\partial}{\partial y}\left\langle 2\nu v\frac{\partial v}{\partial y}\right\rangle_{zt}\right\rangle_{xy}$ is null because $v = 0$ at $y = 0$ and $\frac{\partial v}{\partial y} = 0$ at y=h, and $\left\langle \frac{\partial}{\partial y}\left\langle \nu w\frac{\partial w}{\partial y}\right\rangle_{zt}\right\rangle_{xy}$ is null because $w = 0$ at $y = 0$ and $\frac{\partial w}{\partial y} = 0$ at $y = h$.

The global transport equation for TKE is:

$$\begin{aligned}\left\langle \langle U\rangle_{zt}\frac{\partial\langle k\rangle_{zt}}{\partial x}\right\rangle_{xy} + \left\langle \langle V\rangle_{zt}\frac{\partial\langle k\rangle_{zt}}{\partial y}\right\rangle_{xy} - \left.\left\langle\left\langle \nu u\frac{\partial v}{\partial x}\right\rangle_{zt}\right\rangle_{x}\right|_{y=h} \\ - \left.\left\langle\left\langle \nu w\frac{\partial v}{\partial z}\right\rangle_{zt}\right\rangle_{x}\right|_{y=h} = \langle P_k\rangle_{xyzt} - \langle\epsilon\rangle_{xyzt}\end{aligned} \tag{5.18}$$

but, since some terms are found to be negligible[2], it reduces to:

$$\underbrace{\left\langle \langle uv\rangle_x \frac{\partial\langle U\rangle_x}{\partial y}\right\rangle_{xy}}_{\mathscr{P}_{uv}} + \underbrace{\left\langle \langle vw\rangle_x \frac{\partial\langle W\rangle_x}{\partial y}\right\rangle_{xy}}_{\mathscr{P}_{vw}} = \underbrace{\langle\epsilon\rangle_{xyzt}}_{\mathscr{D}_\epsilon}. \tag{5.19}$$

Eq. (5.19) states that the production terms, $\mathscr{P}_{uv}$ and $\mathscr{P}_{vw}$ are dissipated into heat by the turbulent viscous stresses.

Total kinetic energy balance

The sum of the global transport equations for MKE and TKE leads to the global balance for total mechanic energy:

$$P + P_{in} = \mathscr{D}_U + \mathscr{D}_W + \mathscr{D}_\epsilon \tag{5.20}$$

The energy inputs P and P_{in} spent respectively to drive the flow along x and to enforce the control action, are dissipated into heat through the viscous action of the mean streamwise and spanwise flow gradients, represented by $\mathscr{D}_U$ and $\mathscr{D}_W$, and through the viscous dissipation $\mathscr{D}_\epsilon$ of the turbulent fluctuations.

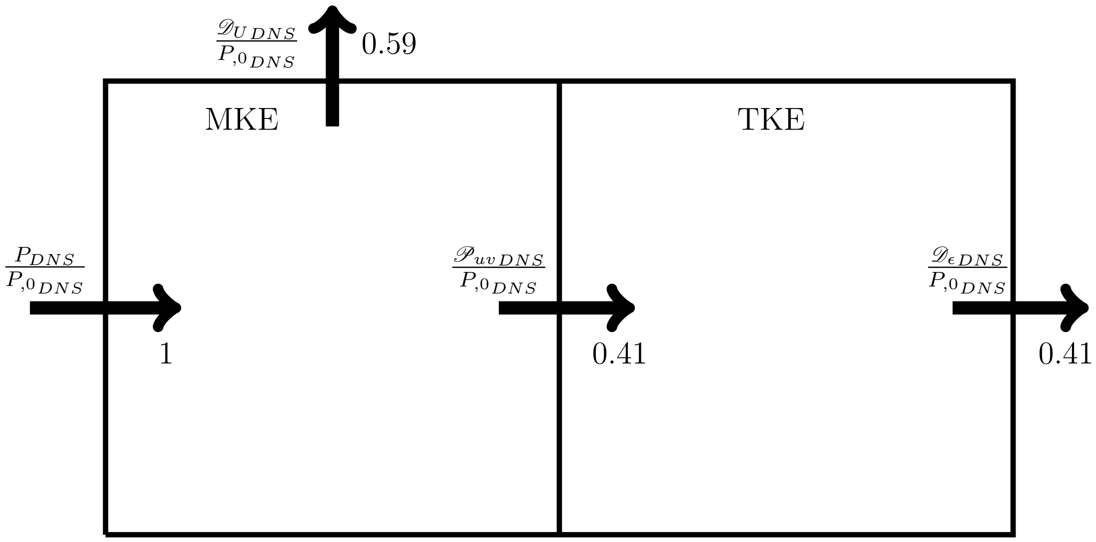
$\frac{\mathscr{D}_{U\,DNS}}{P_{,0_{DNS}}}$
0.59
MKE
TKE
$\frac{P_{DNS}}{P_{,0_{DNS}}}$
1
$\frac{\mathscr{P}_{uv\,DNS}}{P_{,0_{DNS}}}$
0.41
$\frac{\mathscr{D}_{\epsilon\,DNS}}{P_{,0_{DNS}}}$
0.41

Figure 5.2: Energy Box: DNS at $Re_\tau = 200$. The two boxes represent MKE and TKE. The quantities are scaled by the power $P_{,0_{DNS}}$ spent to drive the flow in the streamwise direction in the uncontrolled flow.

In Fig. [5.2] the global energy balance is summarized and quantified in the reference case. The quantities are scaled by the power $P_{,0}{}^{*}_{DNS}$ spent to drive the flow in the streamwise direction in the uncontrolled flow equal to 0.0012. The two boxes represent MKE and TKE. The terms pertaining to the streamwise and spanwise direction are decoupled in MKE and indicated respectively with MKE-x and MKE-z.
In Fig. [5.3] the changes due to the forcing are represented. The terms in the uncontrolled case are indicated by black portion of arrows, whereas the energy transfers due to the forcing are represented by red arrows or portion of arrows. It is clear from the schematic that the production terms $\mathscr{P}_{uv}$ and $\mathscr{P}_{vw}$ disappear from the total energy balance (5.28) because they only transfer energy internally between MKE and TKE. The forcing reduces the value of the not null terms in the reference case, whereas the terms in MKE-z equation only arise if the forcing is applied. Since $\frac{\mathscr{P}_{vw\,DNS}}{P_{,0_{DNS}}} \simeq 0$, it states that the energy input $\frac{P_{DNS}}{P_{,0_{DNS}}}$ is dissipated into heat through $\frac{\mathscr{D}_{U\,DNS}}{P_{,0_{DNS}}}$(43%) and $\frac{\mathscr{D}_{\epsilon\,DNS}}{P_{,0_{DNS}}}$ (57%).

---

[2] $\left\langle \langle U\rangle_{zt}\frac{\partial\langle k\rangle_{zt}}{\partial x}\right\rangle_{xy} \simeq 10^{-7}$; $\left\langle \langle V\rangle_{zt}\frac{\partial\langle k\rangle_{zt}}{\partial y}\right\rangle_{xy} \simeq 10^{-9}$; $\nu\left\langle w\frac{\partial w}{\partial z}\right\rangle_{xzt}\Big|_{y=h} \simeq 10^{-9}$; $\nu\left\langle u\frac{\partial v}{\partial x}\right\rangle_{xzt}\Big|_{y=h} \simeq 10^{-7}$

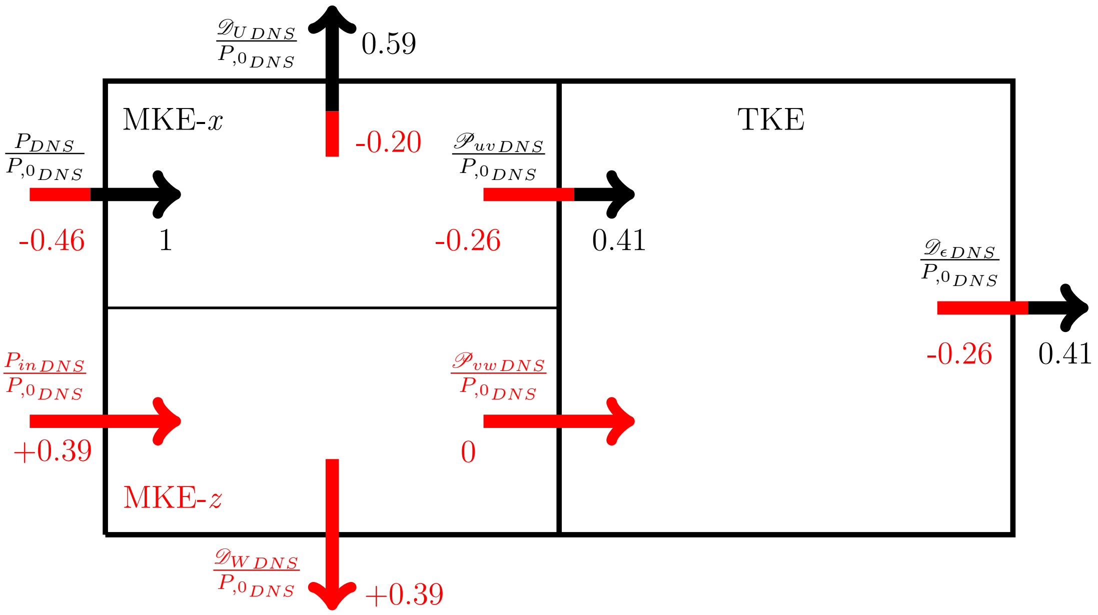
$\frac{\mathscr{D}_{U\,DNS}}{P_{,0\,DNS}}$
0.59
-0.20
MKE-x
TKE
$\frac{P_{DNS}}{P_{,0\,DNS}}$
-0.46
1
$\frac{\mathscr{P}_{uv\,DNS}}{P_{,0\,DNS}}$
-0.26
0.41
$\frac{\mathscr{D}_{\epsilon\,DNS}}{P_{,0\,DNS}}$
-0.26
0.41
$\frac{P_{in\,DNS}}{P_{,0\,DNS}}$
+0.39
$\frac{\mathscr{P}_{vw\,DNS}}{P_{,0\,DNS}}$
0
MKE-z
$\frac{\mathscr{D}_{W\,DNS}}{P_{,0\,DNS}}$
+0.39

Figure 5.3: Energy Box: DNS at $Re_\tau = 200$. *The two boxes represent MKE and TKE. The portion of MKE-x and of MKE-z indicate the portion of the MKE balance pertaining respectively to the streamwise and spanwise direction. The terms in the uncontrolled case are indicated by black portion of arrows, whereas the energy transfers due to the forcing are represented by red arrow or portion of arrows. The quantities are scaled by the power* $P_{,0\,DNS}$ *spent to drive the flow in the streamwise direction in the uncontrolled flow.*

Turbulent viscous dissipation

The turbulent dissipation ϵ is:

$$\begin{aligned}\epsilon = 2\left(\frac{\partial u}{\partial x}\right)^2 + \left(\frac{\partial u}{\partial y}\right)^2 + \left(\frac{\partial u}{\partial z}\right)^2 + \left(\frac{\partial v}{\partial x}\right)^2 \\ +2\left(\frac{\partial v}{\partial y}\right)^2 + \left(\frac{\partial v}{\partial z}\right)^2 + \left(\frac{\partial w}{\partial x}\right)^2 + \left(\frac{\partial w}{\partial y}\right)^2 \\ +2\left(\frac{\partial w}{\partial z}\right)^2 + 2\frac{\partial u}{\partial y}\frac{\partial v}{\partial x} + 2\frac{\partial u}{\partial z}\frac{\partial w}{\partial x} + 2\frac{\partial v}{\partial z}\frac{\partial w}{\partial y}.\end{aligned} \tag{5.21}$$

Once averaged by means of (4.6), it corresponds to term 6 in (5.22).In Fig. [5.4] is shown the ϵ field of half channel, whereas in Fig. [5.5] a section of ϵ is

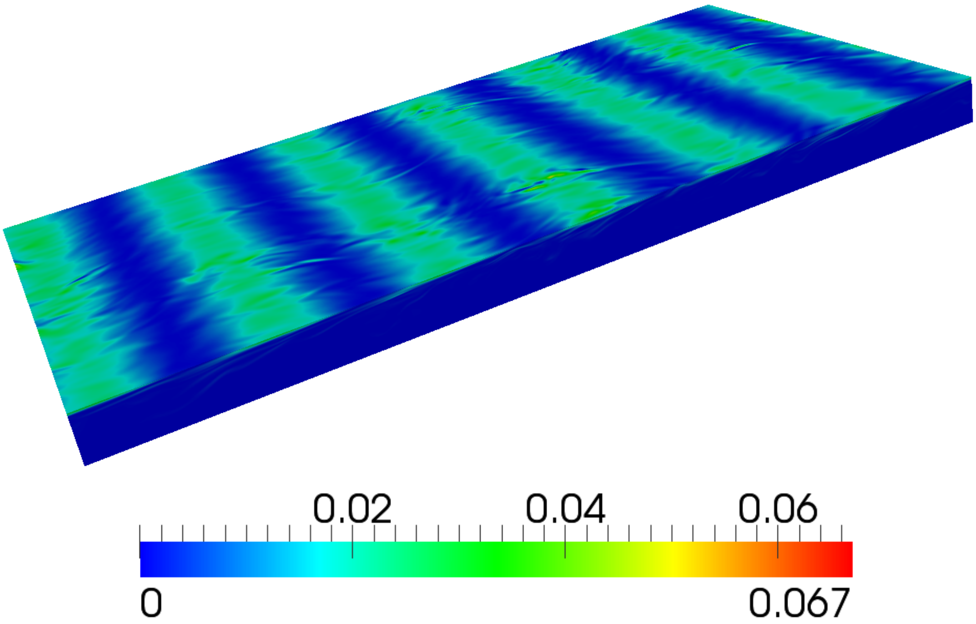

Figure 5.4: Field of the turbulent dissipation ϵ^* calculated via DNS

choose and it will be used to make a comparison with the RANS data. The modulation along the x-direction of this quantity clearly appears.

Turbulent vortical structures

Jeorg and Hussain [19] have introduced the quantity λ_2 in order to identify turbulent vortical structures. In Fig. [5.6] the isosurfaces for λ_2, when the level is set at $\lambda_2^+ = 0.03$ are visualized.

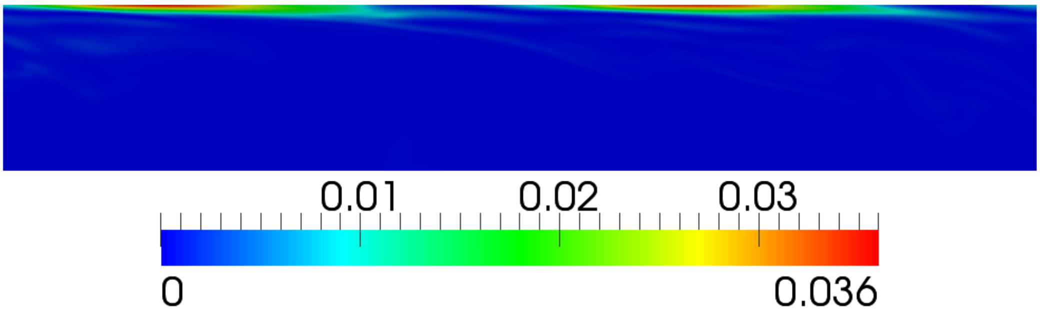

Figure 5.5: Section of the turbulent dissipation ϵ^* field calculated via DNS

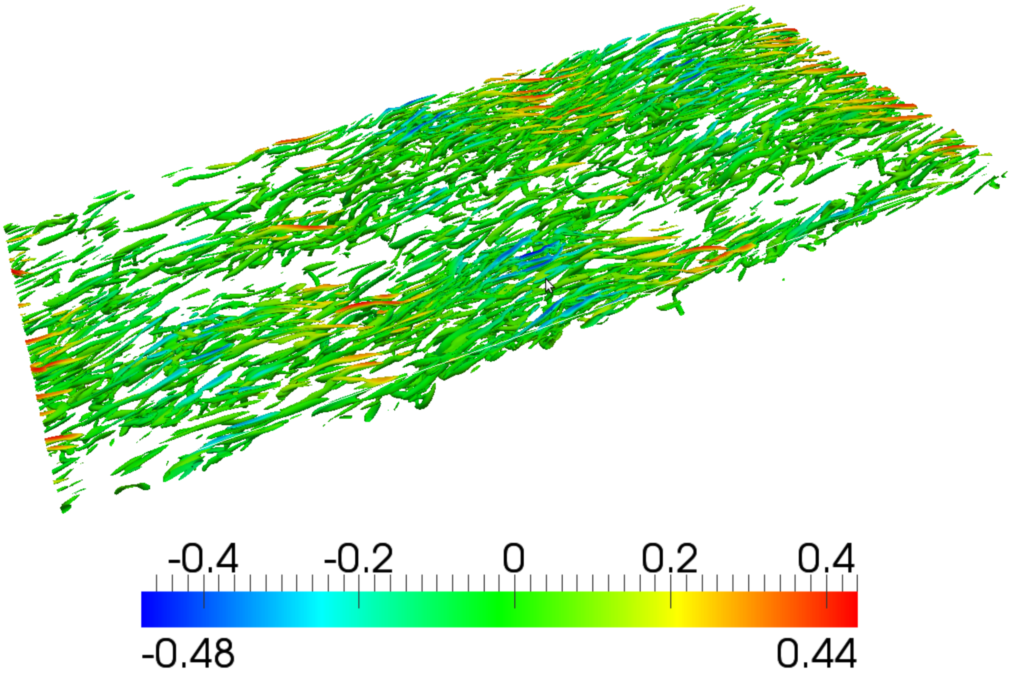
-0.4
-0.2
0
0.2
0.4
-0.48
0.44

Figure 5.6: *Isosurfaces for the quantity* $\lambda_2^+ = -0.03$ *with DNS in the forced case coloured with the spanwise component of the velocity.*

5.2 $\overline{v^2} - f$ model

In Table [5.1] are reported the values of the skin friction coefficient $\langle C_f \rangle_{xzt}$ calculated with the $\overline{v^2} - f$ turbulence model with standard settings for functions and constants. The value of $\langle C_{f,0} \rangle_{xzt}$ is underestimated with a error smaller than 5%. When the forcing is applied the value of $\langle C_f \rangle_{xzt}$ decreases, revealing the ability of the model to predict drag reduction. However the error made in the assessment of $\langle C_{f,0} \rangle_{xzt}$ could positively influence the evaluation of $\langle C_f \rangle_{xzt}$. The computed value of drag reduction rate R is 12.5% when $Re_\tau = 200$ and 6% when $Re_\tau = 1000$, with a percentage error ΔR respectively of -72.1% and of -80% with respect to DNS informations. When the Reynolds number is increased, the error decreases both in reference and in controlled case.

	$\langle C_{f,0} \rangle_{xzt}$	$\Delta C_{f,0}$	$\langle C_f \rangle_{xzt}$	ΔC_f
$Re_\tau = 200$	0.00759	-4.2 %	0.00644	+52.3%
$Re_\tau = 1000$	0.00509	-1.5 %	0.004752	+31.3%

Table 5.1: Values and errors of the skin friction coefficient $\langle C_f \rangle_{xzt}$, in the reference and in the forced case, at $Re_\tau = 200$ and $Re_\tau = 1000$ achieved using the $\overline{v^2} - f$ model.

5.2.1 Mechanism of drag reduction

When a RANS simulation is carried on with $\overline{v^2} - f$ turbulence model, the only difference respect to (5.1.2) is that the TKE equation solved is modelled. However the total kinetic energy balance is unchanged respect to (5.28).

Balance equation for the TKE

The transport equation for TKE, in the $\overline{v^2}-f$ model, reads:

$$\begin{aligned}\underbrace{\langle U\rangle_{zt}\frac{\partial\langle k\rangle_{zt}}{\partial x}}_{1}+\underbrace{\langle V\rangle_{zt}\frac{\partial\langle k\rangle_{zt}}{\partial y}}_{2}-\underbrace{\frac{\partial}{\partial x}\left[\left(\nu+\frac{\langle\nu_T\rangle_{zt}}{\sigma_K}\right)\frac{\partial\langle k\rangle_{zt}}{\partial x}\right]}_{3}\\ -\underbrace{\frac{\partial}{\partial y}\left[\left(\nu+\frac{\langle\nu_T\rangle_{zt}}{\sigma_K}\right)\frac{\partial\langle k\rangle_{zt}}{\partial y}\right]}_{4}=\underbrace{\langle P_k\rangle_{zt}}_{5}-\underbrace{\langle\epsilon\rangle_{zt}}_{6}\end{aligned} \tag{5.22}$$

where $\langle P_k\rangle_{zt}$ is the turbulent kinetic production (5.6), $\sigma_K=1$ is a constant and

$$\langle\nu_T\rangle_{zt}=0.22\left\langle v^2\right\rangle_{zt}max\left(\frac{\langle k\rangle_{zt}}{\langle\epsilon\rangle_{zt}},6\sqrt{\frac{\nu}{\langle\epsilon\rangle_{zt}}}\right). \tag{5.23}$$

The value of $\langle v^2\rangle_{zt}$ is obtained by means of a transport equation (see 3.1.2). Terms 1 and 2 denote the convection of TKE, terms 3 and 4 indicate the diffusion, term 5 is the production of TKE and also appears in MKE as sink. Term 6 is the viscous dissipation of TKE. Analogously to the analysis of the MKE equation, the averaging over x leads to:

$$\left\langle\frac{\partial}{\partial x}\left[\left(\nu+\frac{\langle\nu_T\rangle_{zt}}{\sigma_K}\right)\frac{\partial\langle k\rangle_{zt}}{\partial x}\right]\right\rangle_x=0, \tag{5.24}$$

and the integration along y to:

$$\begin{aligned}\left\langle\frac{\partial}{\partial y}\left[\left(\nu+\frac{\langle\nu_T\rangle_{zt}}{\sigma_K}\right)\frac{\partial\langle k\rangle_{zt}}{\partial y}\right]\right\rangle_{xy}=\left\langle\left(\nu+\frac{\langle\nu_T\rangle_{zt}}{\sigma_K}\right)\frac{\partial\langle k\rangle_{zt}}{\partial y}\right\rangle_x\Bigg|_{y=h}\\ -\left\langle\left(\nu+\frac{\langle\nu_T\rangle_{zt}}{\sigma_K}\right)\frac{\partial\langle k\rangle_{x}}{\partial y}\right\rangle_x\Bigg|_{y=0}=-\left\langle\nu\frac{\partial\langle k\rangle_{zt}}{\partial y}\right\rangle_x\Bigg|_{y=0}.\end{aligned} \tag{5.25}$$

The global transport equation for TKE is:

$$\begin{aligned}\left\langle\langle U\rangle_{zt}\frac{\partial\langle k\rangle_{zt}}{\partial x}\right\rangle_{xy}+\left\langle\langle V\rangle_{zt}\frac{\partial\langle k\rangle_{zt}}{\partial y}\right\rangle_{xy}+\left\langle\nu\frac{\partial\langle k\rangle_{zt}}{\partial y}\right\rangle_x\Bigg|_{y=0}\\ =\langle P_k\rangle_{xyzt}-\langle\epsilon\rangle_{xyzt}\end{aligned} \tag{5.26}$$

but, since some terms are found to be negligible[3], it reduces to:

$$\underbrace{\left\langle\langle uv\rangle_x\frac{\partial\langle U\rangle_x}{\partial y}\right\rangle_{xy}}_{\mathscr{P}_{uv}}+\underbrace{\left\langle\langle vw\rangle_x\frac{\partial\langle W\rangle_x}{\partial y}\right\rangle_{xy}}_{\mathscr{P}_{vw}}=\underbrace{\langle\epsilon\rangle_{xy}}_{\mathscr{D}_\epsilon}, \tag{5.27}$$

---

[3] $\left\langle\langle U\rangle_{zt}\frac{\partial\langle k\rangle_{zt}}{\partial x}\right\rangle_{xy}\simeq 10^{-7}$; $\left\langle\langle V\rangle_{zt}\frac{\partial\langle k\rangle_{zt}}{\partial y}\right\rangle_{xy}\simeq 10^{-9}$; $\left\langle\nu\frac{\partial\langle k\rangle_{zt}}{\partial y}\right\rangle_x\Big|_{y=0}\simeq 10^{-7}$

that is the same equation found in (5.1.2).

Total kinetic energy balance

The sum of the global transport equations for MKE and TKE leads to the global balance for total mechanic energy:

$$P + P_{in} = \mathscr{D}_U + \mathscr{D}_W + \mathscr{D}_\epsilon \tag{5.28}$$

In Fig. [5.7] the global energy balance is summarized and quantified. The quantities are scaled by the power $P_{,0_{DNS}}$ spent to drive the flow in the streamwise direction in the uncontrolled flow calculated via DNS. The forcing reduces the value of the not null terms in the reference case, whereas the terms in MKE-z equation only arise if the forcing is applied.

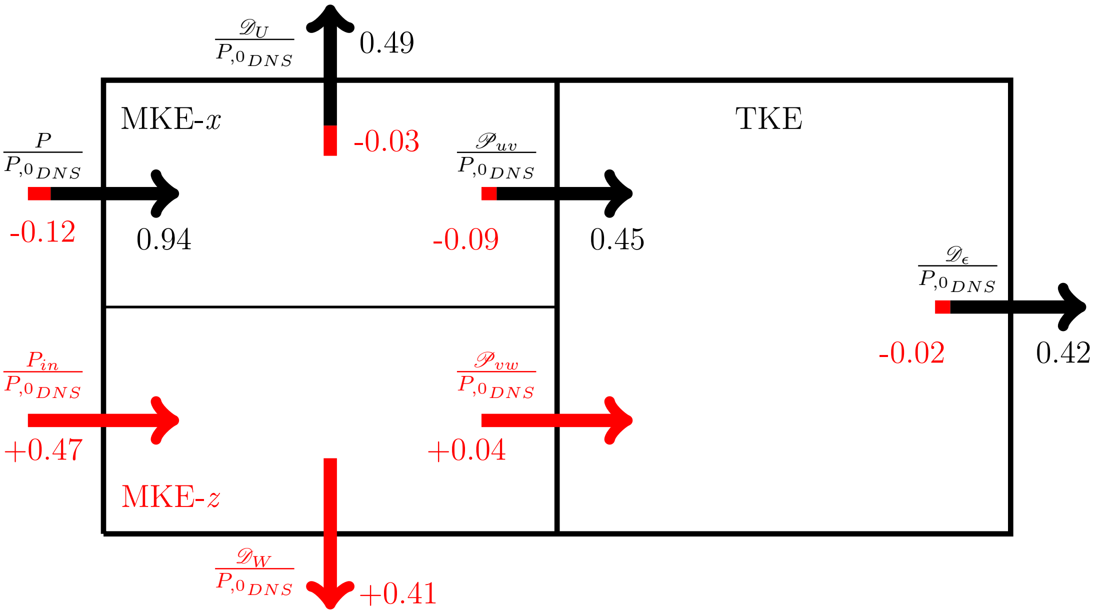
$\frac{\mathscr{D}_U}{P_{,0_{DNS}}}$
0.49
-0.03
MKE-x
TKE
$\frac{P}{P_{,0_{DNS}}}$
-0.12
0.94
$\frac{\mathscr{P}_{uv}}{P_{,0_{DNS}}}$
-0.09
0.45
$\frac{\mathscr{D}_\epsilon}{P_{,0_{DNS}}}$
-0.02
0.42
$\frac{P_{in}}{P_{,0_{DNS}}}$
+0.47
$\frac{\mathscr{P}_{vw}}{P_{,0_{DNS}}}$
+0.04
MKE-z
$\frac{\mathscr{D}_W}{P_{,0_{DNS}}}$
+0.41

Figure 5.7: Energy Box: $\overline{v^2} - f$ model at $Re_\tau = 200$. The quantities are scaled by the power $P_{,0_{DNS}}$ spent to drive the flow in the streamwise direction in the uncontrolled flow calculated via DNS.

To gain insight into the changes of $\langle \tau_w \rangle_{xzt}$ we observe that the turbulence model plays a fundamental role in the prediction of the turbulent viscous dissipation $\langle \epsilon \rangle_{zt}$, therefore indirectly on the terms of MKE-x equation. This leads to an analysis of how and why this modelled quantity is affected by the forcing.

Turbulent viscous dissipation ϵ

The modelled equation for the turbulent dissipation $\langle \epsilon \rangle_{zt}$ is:

$$\begin{aligned}
&\underbrace{\langle U \rangle_{zt} \frac{\partial \langle \epsilon \rangle_{zt}}{\partial x}}_{1} + \underbrace{\langle V \rangle_{zt} \frac{\partial \langle \epsilon \rangle_{zt}}{\partial y}}_{2} - \underbrace{\frac{\partial}{\partial x}\left[\left(\nu + \frac{\langle \nu_T \rangle_{zt}}{\sigma_\epsilon}\right)\frac{\partial \langle \epsilon \rangle_{zt}}{\partial x}\right]}_{3} \\
&\underbrace{-\frac{\partial}{\partial y}\left[\left(\nu + \frac{\langle \nu_T \rangle_{zt}}{\sigma_\epsilon}\right)\frac{\partial \langle \epsilon \rangle_{zt}}{\partial y}\right]}_{4} = \underbrace{\frac{\langle C_{\epsilon 1} \rangle_{zt}}{\langle T \rangle_{zt}} \langle P_k \rangle_{zt}}_{5} - \underbrace{\frac{C_{\epsilon 2}}{\langle T \rangle_{zt}} \langle \epsilon \rangle_{zt}}_{6}
\end{aligned} \tag{5.29}$$

where $\langle \nu_T \rangle_{zt}$ is the turbulent viscosity (5.23), $\langle P_k \rangle_{zt}$ is the turbulent kinetic production (5.6), $\sigma_\epsilon = 1.3$ and $C_{\epsilon 2} = 1.9$ are constants,

$$\langle T \rangle_{zt} = max\left(\frac{\langle k \rangle_{zt}}{\langle \epsilon \rangle_{zt}}, 6\sqrt{\frac{\nu}{\langle \epsilon \rangle_{zt}}}\right), \tag{5.30}$$

and

$$\langle C_{\epsilon 1} \rangle_{zt} = 1.4\left[1 + 0.05\ min\left(\sqrt{\frac{\langle k \rangle_{zt}}{\langle v^2 \rangle_{zt}}}, 100\right)\right]. \tag{5.31}$$

The value of $\langle v^2 \rangle_{zt}$ is obtained by means of a transport equation (see 3.1.2). Analogously to (5.22), terms 1 and 2 denote the convection of turbulent viscous dissipation $\langle \epsilon \rangle_{zt}$, terms 3 and 4 are indicate the diffusion, term 5 and term 6 respectively the production and the viscous dissipation of $\langle \epsilon \rangle_{zt}$. The control acts directly on the turbulent dissipation $\langle \epsilon \rangle_{zt}$, in fact the velocity $\langle W \rangle_{zt}$ appears explicitly in the term 5 of the production. In Fig. [5.8] the modelled quantity $\langle \epsilon \rangle_{zt}$ in the reference case (top) is compared with the one calculated in the forced case (bottom) and in Fig. [5.9] the differences between them are shown in order to highlight the modifications due to the forcing. This mainly acts next to the wall, in the SSL, where a modulation of $\langle \epsilon \rangle_{zt}$ in the x-direction, that is not any more an homogeneous direction once the forcing is applied, is evident.

Fig. [5.10] shows the profiles of the terms in Eq. (5.29) averaged along x-direction in the reference (thin lines) and in the controlled case (thick lines). The term 3 is eliminated by the averaging along x-direction because of space periodicity. The convective terms are null in the reference case and calculated as negligible in the forced one. When the control is realized, the kinetic energy production term is dominant and it is deeply affected by the

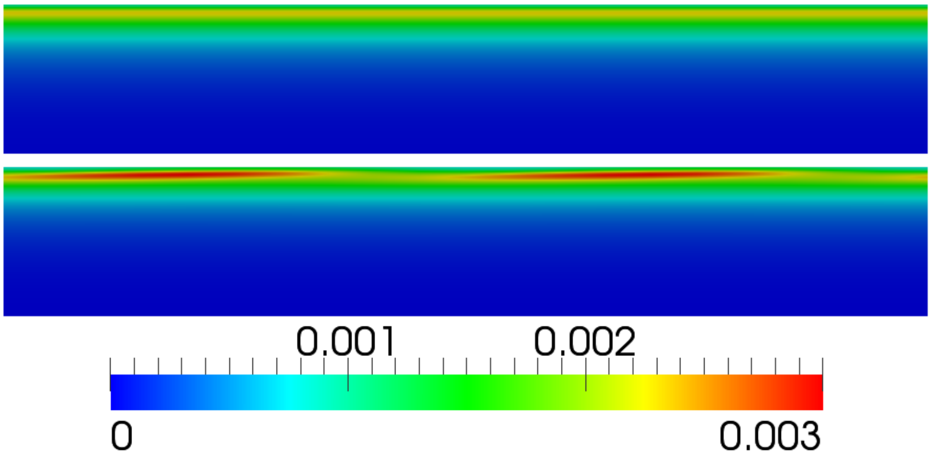

Figure 5.8: Turbulent viscous dissipation $\langle\epsilon\rangle^*_{zt}$ *with* $\overline{v^2} - f$ *model at* $Re_\tau = 200$*: reference case (top) and forced case (below).*

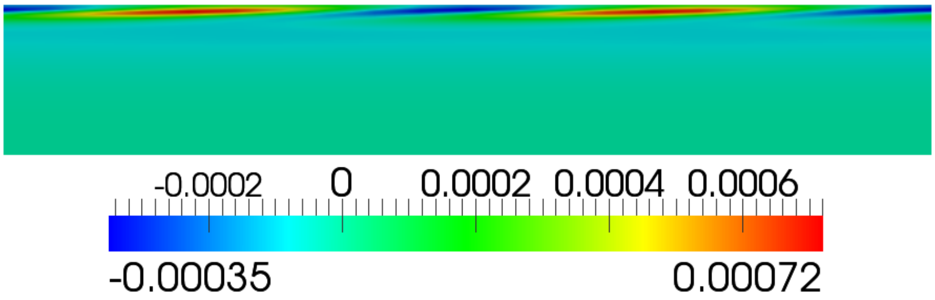

Figure 5.9: Turbulent viscous dissipation $\langle\epsilon\rangle^*_{zt}$ *with* $\overline{v^2} - f$ *model at* $Re_\tau = 200$*: difference between the forced and the reference case.*

forcing: the peak value, reached at $y/h = 0.04$ in both cases, is greater in the forced case. Around this peak production exceeds dissipation and the excess energy produced is transported away by term 4. This term is slightly affected by the forcing and balances the viscous dissipation in a very thin near-wall layer, $y/h < 0.01$, where term 5 is small.

The single components of the turbulent dissipation $\langle\epsilon\rangle_{zt}$ production terms,

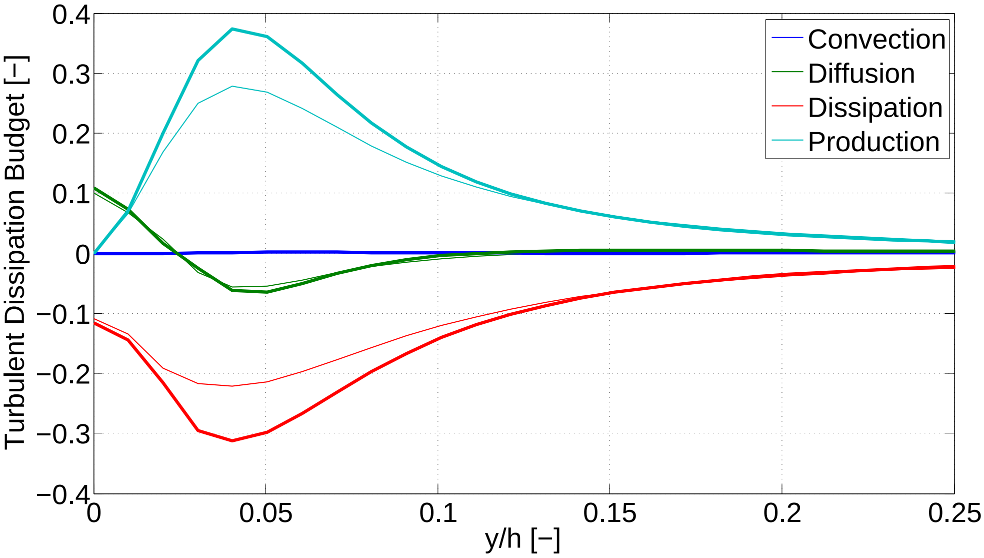

Figure 5.10: Turbulent dissipation budget with $\overline{v^2} - f$ *model at* $Re_\tau = 200$*: terms in Eq. (5.29) averaged along* x*-direction. Reference case (thin lines) and forced case (thick lines).*

once averaged over x, are:

$$\left\langle \frac{\langle C_{\epsilon 1}\rangle_{zt}}{\langle T\rangle_{zt}} \langle P_k\rangle_{zt} \right\rangle_x = -\underbrace{\left\langle \frac{\langle C_{\epsilon 1}\rangle_{zt}}{\langle T\rangle_{zt}} \langle uu\rangle_{zt} \frac{\partial \langle U\rangle_{zt}}{\partial x} \right\rangle_x}_{\mathscr{P}_{\epsilon,uu}} - \underbrace{\left\langle \frac{\langle C_{\epsilon 1}\rangle_{zt}}{\langle T\rangle_{zt}} \langle uv\rangle_{zt} \frac{\partial \langle U\rangle_{zt}}{\partial y} \right\rangle_x}_{\mathscr{P}_{\epsilon,uv}}$$
$$- \underbrace{\left\langle \frac{\langle C_{\epsilon 1}\rangle_{zt}}{\langle T\rangle_{zt}} \langle uv\rangle_{zt} \frac{\partial \langle V\rangle_{zt}}{\partial x} \right\rangle_x}_{\mathscr{P}_{\epsilon,vu}} - \underbrace{\left\langle \frac{\langle C_{\epsilon 1}\rangle_{zt}}{\langle T\rangle_{zt}} \langle vv\rangle_{zt} \frac{\partial \langle V\rangle_{zt}}{\partial y} \right\rangle_x}_{\mathscr{P}_{\epsilon,vv}}$$
$$- \underbrace{\left\langle \frac{\langle C_{\epsilon 1}\rangle_{zt}}{\langle T\rangle_{zt}} \langle uw\rangle_{zt} \frac{\partial \langle W\rangle_{zt}}{\partial x} \right\rangle_x}_{\mathscr{P}_{\epsilon,u}} - \underbrace{\left\langle \frac{\langle C_{\epsilon 1}\rangle_{zt}}{\langle T\rangle_{zt}} \langle vw\rangle_{zt} \frac{\partial \langle W\rangle_{zt}}{\partial y} \right\rangle_x}_{\mathscr{P}_{\epsilon,vw}}, \tag{5.32}$$

Since some terms are found as empirically negligible[4], the relevant terms are $\mathscr{P}_{\epsilon,vw}$ and $\mathscr{P}_{\epsilon,uv}$. They are shown in Fig. [5.11]. The first term, where

---

[4] $\left\langle \frac{\langle C_{\epsilon 1}\rangle_{zt}}{\langle T\rangle_{zt}} \langle uu\rangle_{zt} \frac{\partial \langle U\rangle_{zt}}{\partial x} \right\rangle_x \simeq 10^{-4}$;$\left\langle \frac{\langle C_{\epsilon 1}\rangle_{zt}}{\langle T\rangle_{zt}} \langle uv\rangle_{zt} \frac{\partial \langle V\rangle_{zt}}{\partial x} \right\rangle_x \simeq 10^{-6}$; $\left\langle \frac{\langle C_{\epsilon 1}\rangle_{zt}}{\langle T\rangle_{zt}} \langle vv\rangle_{zt} \frac{\partial \langle V\rangle_{zt}}{\partial y} \right\rangle_x \simeq 10^{-4}$;$\left\langle \frac{\langle C_{\epsilon 1}\rangle_{zt}}{\langle T\rangle_{zt}} \langle uw\rangle_{zt} \frac{\partial \langle W\rangle_{zt}}{\partial x} \right\rangle_x \simeq 10^{-3}$

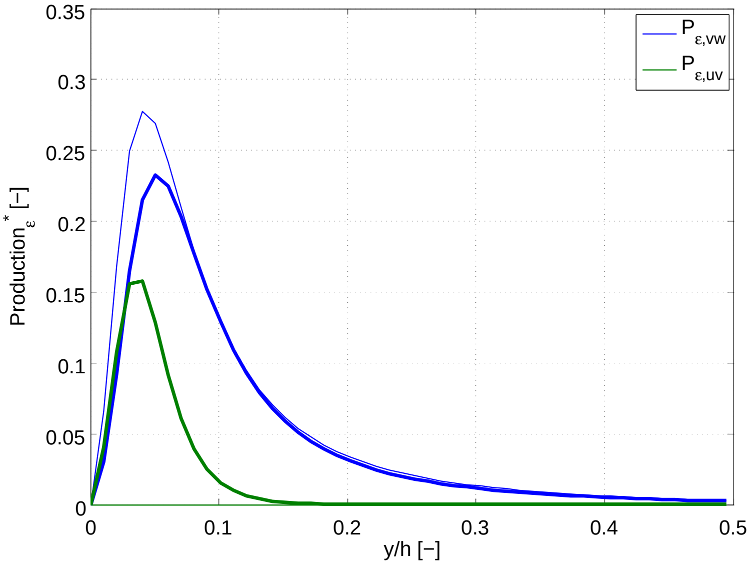

Figure 5.11: Production terms of $\langle \epsilon \rangle_{zt}$, *calculated with* $\overline{v^2} - f$ *model at* $Re_\tau = 200$, *averaged in* x*-direction in (5.32). Reference case (thin lines) and forced case (thick lines).*

$\langle W\rangle_{zt}$ explicitly appears, is absent in the reference case because both $\langle vw\rangle_{zt}$ and $\langle W\rangle_{zt}$ are null. The second term corresponds to the $\langle\epsilon\rangle_{zt}$ production when the control is not applied, being the only one not null. It is indirectly modified by the forcing: its peak decreases and moves upward.
It could be observed that:

$$\frac{\langle C_{\epsilon 1}\rangle_{zt}}{\langle T\rangle_{zt}}\mathscr{P}_{uv} = \underbrace{\frac{\langle C_{\epsilon 1}\rangle_{zt}}{\langle T\rangle_{zt}}\langle uv\rangle_{zt}}_{A}\underbrace{\frac{\partial\langle U\rangle_{zt}}{\partial y}}_{B} \tag{5.33}$$

where, since term A is slightly affected by the forcing, the modifications are mainly linked to the change of term B[5].

In conclusion the change of $\langle\epsilon\rangle_{zt}$ is directly linked to $\left\langle\frac{\langle C_{\epsilon 1}\rangle_{zt}}{\langle T\rangle_{zt}}\mathscr{P}_{vw}\right\rangle_x$ and indirectly linked to $\left\langle\frac{\langle C_{\epsilon 1}\rangle_{zt}}{\langle T\rangle_{zt}}\mathscr{P}_{uv}\right\rangle_x$, where in particular the quantity $\frac{\partial\langle U\rangle_{zt}}{\partial y}$ is affected by the forcing. This quantity plays a important rule in the MKE-x equation leading to a change of $\langle\tau_w\rangle_{xzt}$ since U_b and ρ are constant quantities.

$$\underbrace{-\frac{U_b}{\rho}\langle\tau_w\rangle_{xzt}}_{P} = \underbrace{\left\langle\langle uv\rangle_{zt}\frac{\partial\langle U\rangle_{zt}}{\partial y}\right\rangle_{xy}}_{\mathscr{P}_{uv}} - \underbrace{\left\langle\nu\left(\frac{\partial\langle U\rangle_{zt}}{\partial y}\right)^2\right\rangle_{xy}}_{\mathscr{D}_U}. \tag{5.34}$$

Comparison with DNS data

The percentage errors made by the turbulence model are calculated by means of Eq. (5.1) and they are reported in Fig. [5.12]. Because of $\frac{\mathscr{P}_{uwDNS}}{P_{,0_{DNS}}}$ is null in the DNS data the percentage error made tends to infinity. In the reference case the errors are less than 20% whereas when the control is applied the errors reach relevant values, especially the error committed in the $\langle\epsilon\rangle_{zt}$ valuation.

In Fig. [5.14] shows a section of the turbulent dissipation field calculated via DNS (top) and the field $\langle\epsilon\rangle_{zt}$ calculated via RANS (bottom). Although the comparison is only qualitative clearly emerges that the error made by the turbulence model $\overline{v^2}-f$ in the assessment of $\langle\epsilon\rangle_{zt}$ is relevant, confirming the results in Fig. [5.12]. However by making a qualitative comparison between the top figure in Fig. [5.14] and the bottom figure in Fig. [5.8], where the $\langle\epsilon\rangle_{zt}$ field with $\overline{v^2}-f$ is shown with the appropriate scale, emerges

---

[5] $A - A_{,0}$: max$\simeq 10^{-4}$, min$\simeq 10^{-7}$; $B - B_{,0}$: max$\simeq 2.6$; min$=\simeq -7.5$

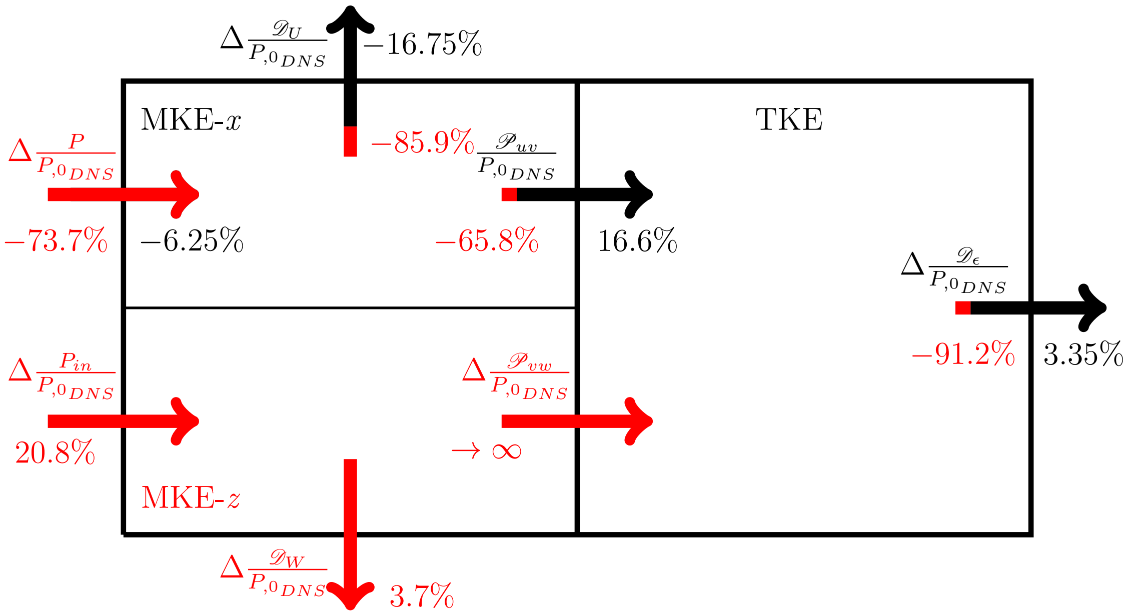
$\Delta\frac{\mathscr{D}_U}{P_{,0_{DNS}}}$
-16.75%
MKE-x
TKE
$\Delta\frac{P}{P_{,0_{DNS}}}$
-85.9%
$\Delta\frac{\mathscr{P}_{uv}}{P_{,0_{DNS}}}$
-73.7%
-6.25%
-65.8%
16.6%
$\Delta\frac{\mathscr{D}_\epsilon}{P_{,0_{DNS}}}$
-91.2%
3.35%
$\Delta\frac{P_{in}}{P_{,0_{DNS}}}$
$\Delta\frac{\mathscr{P}_{vw}}{P_{,0_{DNS}}}$
20.8%
$\to\infty$
MKE-z
$\Delta\frac{\mathscr{D}_W}{P_{,0_{DNS}}}$
3.7%

Figure 5.12: Energy Box: Percentage error committed by $\overline{v^2}-f$ at $Re_\tau = 200$.

that the turbulent model includes the existing modulation in x direction, although differences exist: the maximum value of $\langle\epsilon\rangle_{zt}$ is reached at the wall in the DNS whereas next to it in the RANS where the prolongations in the streamwise directions are not visible.

In Fig. [5.23] is shown the SSL achieved via DNS and via RANS when the spanwise velocity reaches its maximum value. A good accordance is found, however the comparison is only qualitative because the SSL calculated with DNS is not averaged along the homogeneous direction z and time t.

5.3 Launder Sharma $k-\epsilon$ model

The values of the skin friction coefficient $\langle C_f\rangle_{xzt}$ computed using the Launder Sharma $k-\epsilon$ turbulence model are in Table [5.2]. The value of $\langle C_{f,0}\rangle_{xzt}$ is understimated both at $Re_\tau = 200$ and $Re_\tau = 1000$, whereas the value of $\langle C_f\rangle_{xzt}$ is overestimate at $Re_\tau = 1000$. The calculated value of drag reduction rate $\langle R\rangle$ is 30.5% when $Re_\tau = 200$ and 27.7% when $Re_\tau = 1000$, with a percentage error ΔR respectively of -32.3% and of -7.5% with respect to DNS data. When the Reynolds number is increased the error committed both in the reference and in the controlled case decreases.

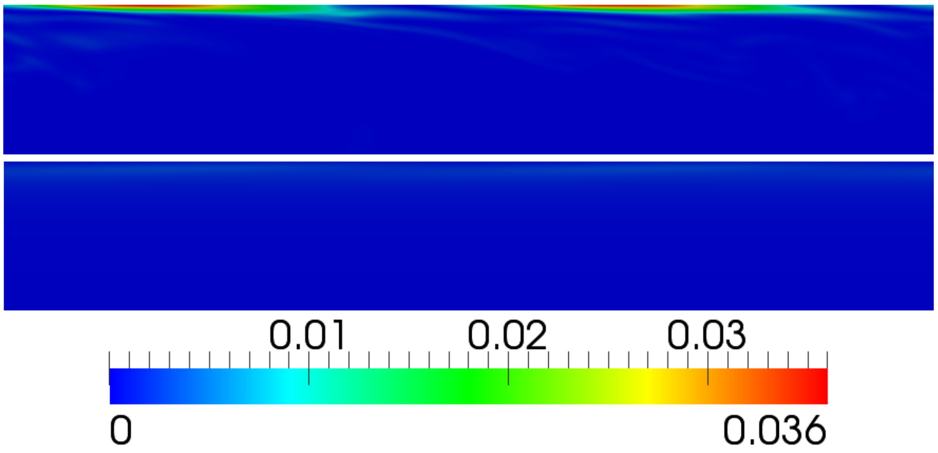

Figure 5.13: Qualitative comparison between a section of the turbulent dissipation field ϵ^* calculated with DNS (top) and the averaged one $\langle\epsilon^*\rangle_{zt}$ calculated with $\overline{v^2} - f$ model (bottom).

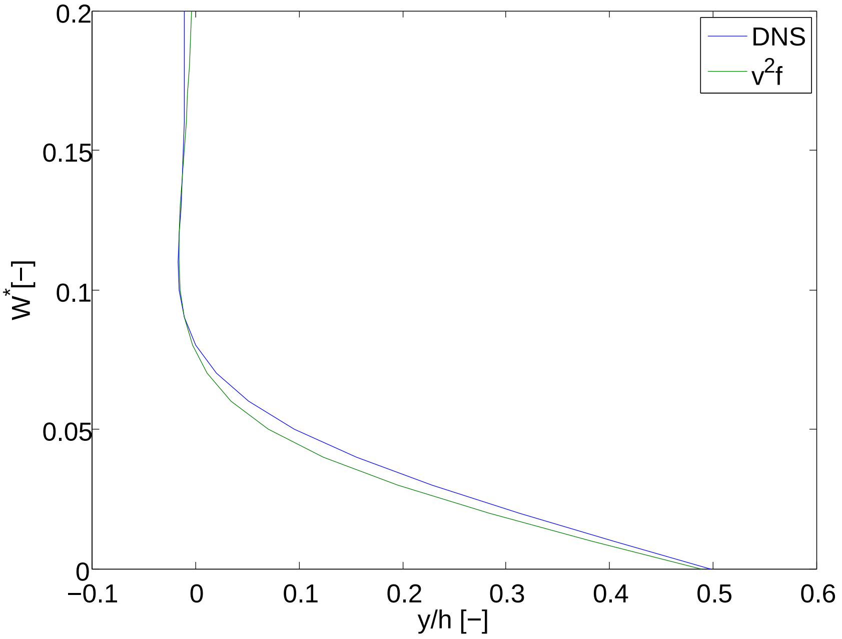

Figure 5.14: Qualitative comparison between the SSL calculated with DNS and the one calculated with $\overline{v^2} - f$ model.

	$\langle C_{f,0}\rangle_{xzt}$	$\Delta C_{f,0}$	$\langle C_f\rangle_{xzt}$	ΔC_f
$Re_\tau = 200$	0.00705	-11.1%	0.0049	+13%
$Re_\tau = 1000$	0.00465	-10%	0.00336	-7.1%

Table 5.2: Values and errors of the skin friction coefficient $\langle C_f\rangle_{xzt}$ in the reference and in the forced case at $Re_\tau = 200$ and $Re_\tau = 1000$ with the Launder Sharma $k-\epsilon$ model.

5.3.1 Prediction of drag reduction

The balances of MKE and TKE have been analysed in section (5.1.2) and (5.2.1) and the same considerations as before are effective. In Fig. [5.15] the global energy balance is summarized and quantified. The value of $\mathscr{P}_{uv}$ is really small thus the energy input P is mainly dissipated by ϵ and $\mathscr{D}_U$. All the quantities not null in the reference case decrease because of the forcing.

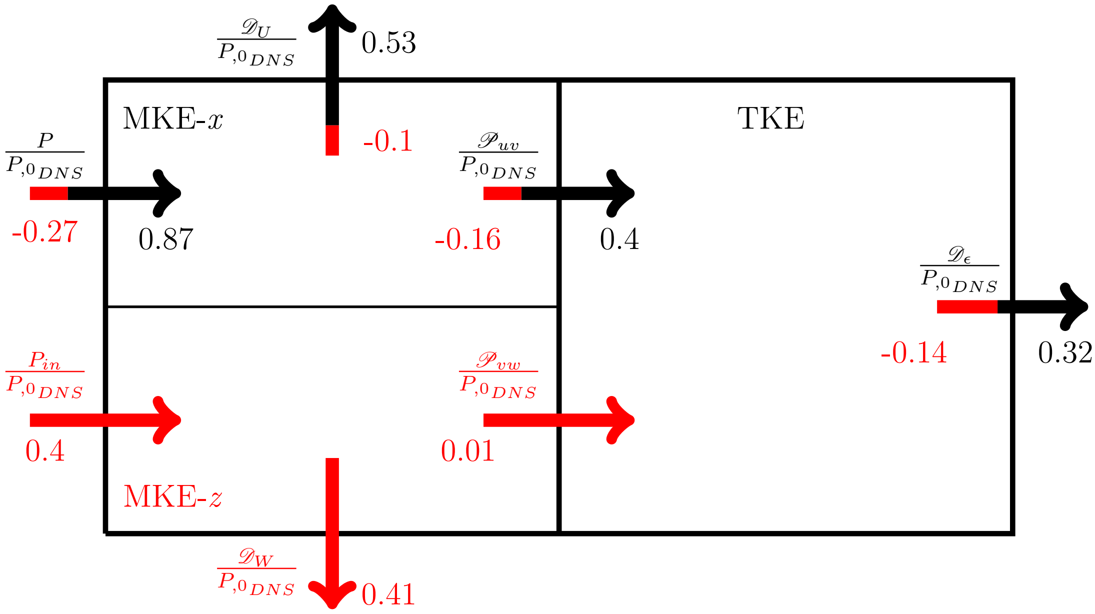
$\frac{\mathscr{D}_U}{P_{,0\,DNS}}$
0.53
-0.1
MKE-x
TKE
$\frac{P}{P_{,0\,DNS}}$
-0.27
0.87
$\frac{\mathscr{P}_{uv}}{P_{,0\,DNS}}$
-0.16
0.4
$\frac{\mathscr{D}_\epsilon}{P_{,0\,DNS}}$
-0.14
0.32
$\frac{P_{in}}{P_{,0\,DNS}}$
0.4
$\frac{\mathscr{P}_{vw}}{P_{,0\,DNS}}$
0.01
MKE-z
$\frac{\mathscr{D}_W}{P_{,0\,DNS}}$
0.41

Figure 5.15: Energy Box calculated with Launder Sharma $k-\epsilon$ model at $Re_\tau = 200$.

Turbulent viscous dissipation ϵ

In the Launder Sharma $k-\epsilon$ turbulence model the turbulent viscous dissipation is:

$$\langle \epsilon \rangle_{zt} = \langle \tilde{\epsilon} \rangle_{zt} + \langle D \rangle_{zt} \,, \tag{5.35}$$

where $\langle D \rangle_{zt} = 2\nu \left(\frac{\partial \sqrt{\langle k \rangle_{zt}}}{\partial x} \right)^2 + 2\nu \left(\frac{\partial \sqrt{\langle k \rangle_{zt}}}{\partial y} \right)^2 + 2\nu \left(\frac{\partial \sqrt{\langle k \rangle_{zt}}}{\partial z} \right)^2$. In Fig. [5.16] the fields of $\langle \epsilon \rangle_{zt}$ in the reference case (top) and in the forced one (bottom) are compared, whereas in Fig. [5.17] the differences between them are shown in order to highlight the modifications due to the control. The forcing, acting mainly into the SSL, halve the maximum value of $\langle \epsilon \rangle_{zt}$ and moves the peaks upward.

With the aim of understanding how the quantity $\langle \epsilon \rangle_{zt}$ is affected by the forcing we first observe that the extra term $\langle D \rangle_{zt}$ is slightly influenced by the forcing. The difference between the reference and the forced case is shown in Fig. [5.18]. It is then clear that the quantity $\langle \tilde{\epsilon} \rangle_{zt}$ is mainly accountable for the change of $\langle \epsilon \rangle_{zt}$. The modelled equation for $\langle \tilde{\epsilon} \rangle_{zt}$ in Launder Sharma

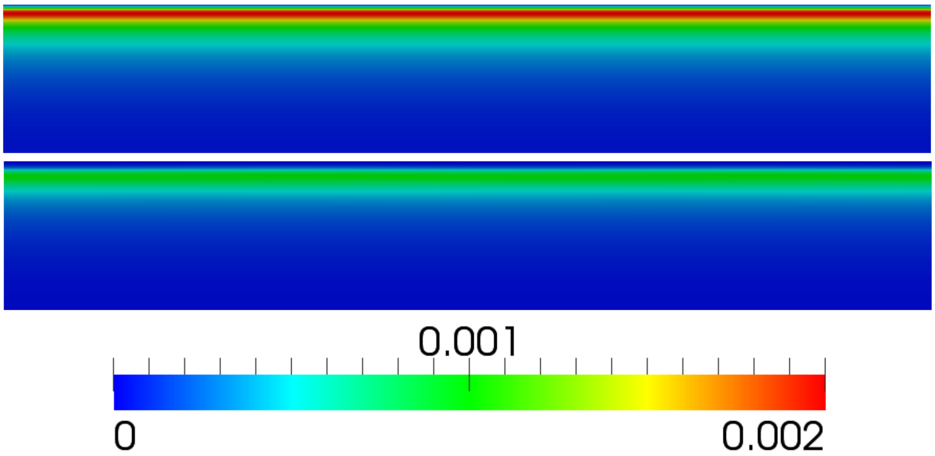

Figure 5.16: Turbulent viscous dissipation $\langle \epsilon \rangle_{zt}^{*}$ *with Launder Sharma* $k-\epsilon$ *model at* $Re_\tau = 200$*: comparison between reference case (top) and forced one (bottom)*

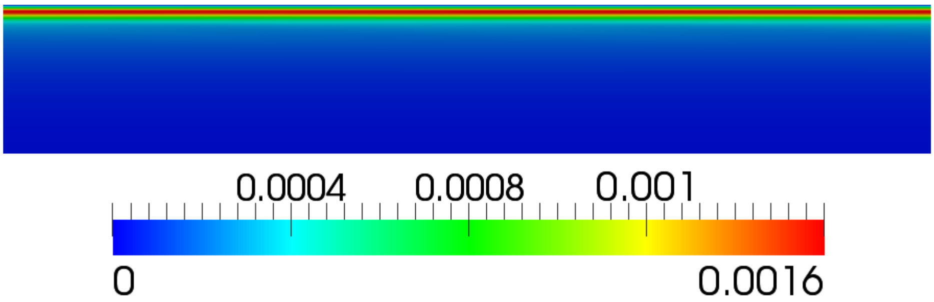

Figure 5.17: Turbulent viscous dissipation $\langle \epsilon \rangle_{zt}^{*}$ *with Launder Sharma* $k-\epsilon$ *model at* $Re_\tau = 200$*: difference between forced and reference case.*

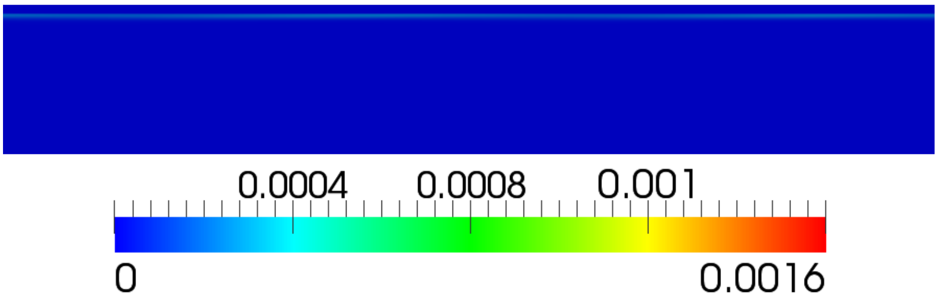

Figure 5.18: Turbulent dissipation with Launder Sharma $k-\epsilon$ *model: difference of term* $\langle D \rangle_{zt}$ *between the forced and the reference case.*

$k-\epsilon$ is:

$$\underbrace{\langle U \rangle_{zt} \frac{\partial \langle \tilde{\epsilon} \rangle_{zt}}{\partial x}}_{1} + \underbrace{\langle V \rangle_{zt} \frac{\partial \langle \tilde{\epsilon} \rangle_{zt}}{\partial y}}_{2} - \underbrace{\frac{\partial}{\partial x}\left[\left(\nu + \frac{\langle \nu_T \rangle_{zt}}{\sigma_\epsilon}\right) \frac{\partial \langle \tilde{\epsilon} \rangle_{zt}}{\partial x}\right]}_{3}$$
$$- \underbrace{\frac{\partial}{\partial y}\left[\left(\nu + \frac{\langle \nu_T \rangle_{zt}}{\sigma_\epsilon}\right) \frac{\partial \langle \tilde{\epsilon} \rangle_{zt}}{\partial y}\right]}_{4} = \underbrace{1.44 \langle P_k \rangle_{zt} \frac{\langle \tilde{\epsilon} \rangle_{zt}}{\langle k \rangle_{zt}}}_{5} -$$
$$\underbrace{1.92 \left(1 - 0.3 e^{{\frac{\langle k \rangle_{zt}^{2}}{\nu \langle \tilde{\epsilon} \rangle_{zt}}}^{2}}\right) \frac{\langle \tilde{\epsilon} \rangle_{zt}}{\langle k \rangle_{zt}}}_{6} + \underbrace{2\nu \langle \nu_T \rangle_{zt} \left[\frac{\partial^2 \langle U \rangle_{zt}}{\partial x \partial x} + \frac{\partial^2 \langle U \rangle_{zt}}{\partial x \partial y} + \frac{\partial^2 \langle V \rangle_{zt}}{\partial x \partial y} + \frac{\partial^2 \langle V \rangle_{zt}}{\partial y \partial y}\right]}_{7} \tag{5.36}$$

where analogously to (5.29) term 1 and 2 denote the convection of $\langle \tilde{\epsilon} \rangle_{zt}$, term 3 and 4 indicate diffusion, term 5 and term 6 respectively the production and the of $\langle \tilde{\epsilon} \rangle_{zt}$. Here appears term 7 that has been introduced in this model in order to improve prediction in the wall region. The velocity $\langle W \rangle_{zt}$ appears

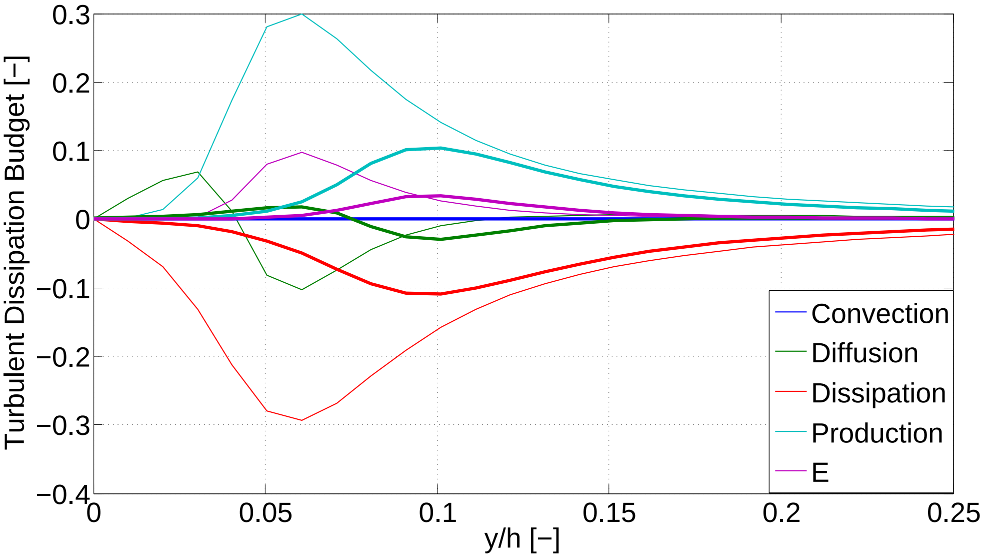

Figure 5.19: Turbulent dissipation budget with Launder Sharma $k-\epsilon$ model: terms of (5.36) averaged in x-direction. Reference case (thin lines) and forced case (thick lines).

explicitly in the term 5 of the production, where $\langle P_k \rangle_{zt}$ is Eq. (5.6). This indicates that the control acts directly on $\langle \tilde{\epsilon} \rangle_{zt}$.

In Fig. [5.19] are shown the profiles of the terms (5.36) averaged in x-direction in the reference (thin lines) and the controlled case (thick lines). The convection terms are null in the reference case and negligible in the forced one, whereas term 3 is null once averaged along x-direction because of space periodicity. When the control is actuated, peaks of each quantity decrease and move upward. In particular the production term is a quantity deeply affected by the forcing.

The single components of this term are shown in Fig. [5.20]. Since some terms are found to be negligible[6], the only relevant terms are $1.44 \left\langle \langle uw \rangle_{zt} \frac{\partial \langle W \rangle_{zt}}{\partial x} \frac{\langle \tilde{\epsilon} \rangle_{zt}}{\langle k \rangle_{zt}} \right\rangle_x$ and $1.44 \left\langle \langle uv \rangle_{zt} \frac{\partial \langle U \rangle_{zt}}{\partial y} \frac{\langle \tilde{\epsilon} \rangle_{zt}}{\langle k \rangle_{zt}} \right\rangle_x$. The first term, where $\langle W \rangle_{zt}$ explicitly appears, is absent in the reference case because both $\langle vw \rangle_{zt}$ and $\langle W \rangle_{zt}$ are null. The second term corresponds to the production when the control is not applied,

---

[6] $1.44 \left\langle \langle uu \rangle_{zt} \frac{\partial \langle U \rangle_{zt}}{\partial x} \frac{\langle \tilde{\epsilon} \rangle_{zt}}{\langle k \rangle_{zt}} \right\rangle_x \simeq -10^{-8}$; $1.44 \left\langle \langle uv \rangle_{zt} \frac{\partial \langle V \rangle_{zt}}{\partial x} \frac{\langle \tilde{\epsilon} \rangle_{zt}}{\langle k \rangle_{zt}} \right\rangle_x \simeq -10^{-9}$; $1.44 \left\langle \langle vv \rangle_{zt} \frac{\partial \langle V \rangle_{zt}}{\partial y} \frac{\langle \tilde{\epsilon} \rangle_{zt}}{\langle k \rangle_{zt}} \right\rangle_x \simeq 10^{-8}$; $1.44 \left\langle \langle uw \rangle_{zt} \frac{\partial \langle W \rangle_{zt}}{\partial x} \frac{\langle \tilde{\epsilon} \rangle_{zt}}{\langle k \rangle_{zt}} \right\rangle_x \simeq -10^{-8}$;

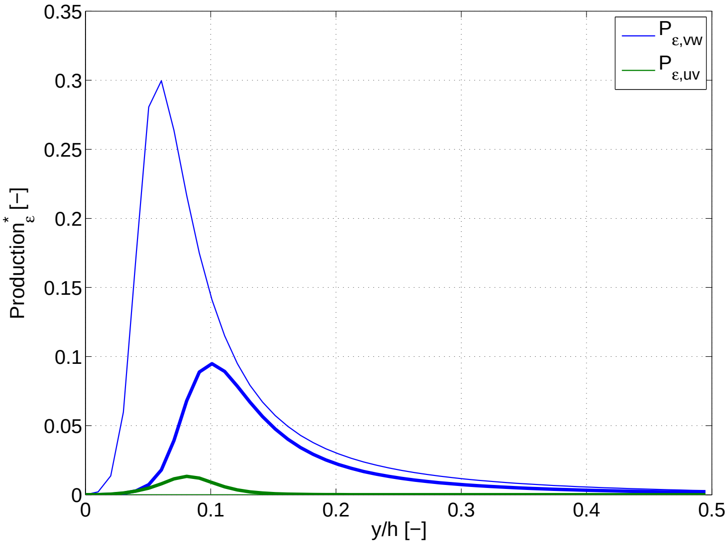

Figure 5.20: Launder Sharma $k-\epsilon$ model. Production terms of $\langle\tilde{\epsilon}\rangle_{zt}$ averaged in x*-direction. Reference case (thin lines) and forced case (thick lines).*

being the only not null one. It is indirectly modified by the forcing: its peak decreases and moves upward. It could be observed that:

$$1.44\left\langle \langle uv\rangle_{zt}\frac{\partial\langle U\rangle_{zt}}{\partial y}\frac{\langle\tilde{\epsilon}\rangle_{zt}}{\langle k\rangle_{zt}}\right\rangle_x = \underbrace{1.44\frac{\langle\tilde{\epsilon}\rangle_{zt}}{\langle T\rangle_{zt}}\langle uv\rangle_{zt}}_{A}\underbrace{\frac{\partial\langle U\rangle_{zt}}{\partial y}}_{B} \tag{5.37}$$

where, since term A is slightly affected by the forcing, the modifications are mainly linked to the change of term B[7]. In conclusion the change of ϵ is directly linked to $1.44\left\langle \langle uw\rangle_{zt}\frac{\partial\langle W\rangle_{zt}}{\partial x}\frac{\langle\tilde{\epsilon}\rangle_{zt}}{\langle k\rangle_{zt}}\right\rangle_x$ and indirectly linked to $1.44\left\langle \langle uv\rangle_{zt}\frac{\partial\langle U\rangle_{zt}}{\partial y}\frac{\langle\tilde{\epsilon}\rangle_{zt}}{\langle k\rangle_{zt}}\right\rangle_x$, where in particular the quantity $\frac{\partial\langle U\rangle_{zt}}{\partial y}$ is affected by the forcing. This quantity plays an important rule in the MKE-x equation leading to a change of $\langle\tau_w\rangle_{xzt}$ since U_b and ρ are constant quantities.

$$\underbrace{-\frac{U_b}{\rho}\langle\tau_w\rangle_{xzt}}_{P} = \underbrace{\left\langle \langle uv\rangle_{zt}\frac{\partial\langle U\rangle_{zt}}{\partial y}\right\rangle_{xy}}_{\mathscr{P}_{uv}} - \underbrace{\left\langle \nu\left(\frac{\partial\langle U\rangle_{zt}}{\partial y}\right)^2\right\rangle_{xy}}_{\mathscr{D}_U}. \tag{5.38}$$

---

[7] $A-A_{,0}$: max$\simeq 10^{-3}$, min$\simeq 10^{-19}$; $B-B_{,0}$: max$\simeq 11$; min$=\simeq -17$

Comparison with DNS data

Starting from the DNS data in Fig. [5.5] the results given by the Launder Sharma $k-\epsilon$ turbulence model are analysed. Because $\frac{\mathscr{P}_{uw DNS}}{P_{,0_{DNS}}}$ is null in the DNS data the percentage error made tends to infinity. In the reference case the errors are about 20% whereas when the control is applied the errors reach relevant values.

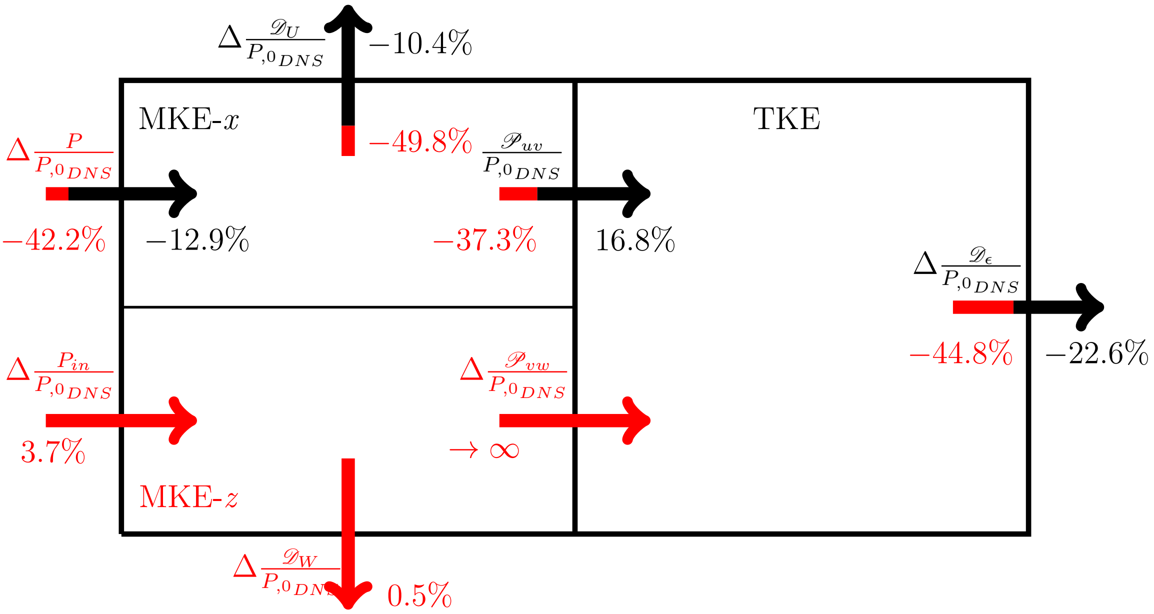
$\Delta \frac{\mathscr{D}_U}{P_{,0_{DNS}}}$
-10.4%
MKE-x
-49.8%
$\frac{\mathscr{P}_{uv}}{P_{,0_{DNS}}}$
TKE
$\Delta \frac{P}{P_{,0_{DNS}}}$
-42.2%
-12.9%
-37.3%
16.8%
$\Delta \frac{\mathscr{D}_\epsilon}{P_{,0_{DNS}}}$
-44.8%
-22.6%
$\Delta \frac{P_{in}}{P_{,0_{DNS}}}$
3.7%
$\Delta \frac{\mathscr{P}_{vw}}{P_{,0_{DNS}}}$
$\rightarrow \infty$
MKE-z
$\Delta \frac{\mathscr{D}_W}{P_{,0_{DNS}}}$
0.5%

Figure 5.21: Energy Box: Percentage error committed by Launder Sharma $k-\epsilon$ *at* $Re_\tau = 200$.

In Fig. [5.22] the turbulent disspation ϵ field calculated via DNS (top) is qualitatively compared with the averaged one achieved via RANS (bottom) when the control is realized. As known from the value in the energy box, the Launder Sharma $k-\epsilon$ is unable to model correctly $\langle\epsilon\rangle_{zt}$ so the results are quantitatively wrong. Ever more so comparison between the top figure in Fig. [5.22] and the bottom figure in Fig. [5.16], where the $\langle\epsilon\rangle_{zt}$ field with Launder Sharma $k-\epsilon$ is shown with the appropriate scale, emerges that the turbulent model does not even include the existing modulation in x-direction.

In Fig. [5.23] is shown the SSL achieved via DNS and via RANS when the spanwise velocity reaches its maximum value. A good accordance is found,

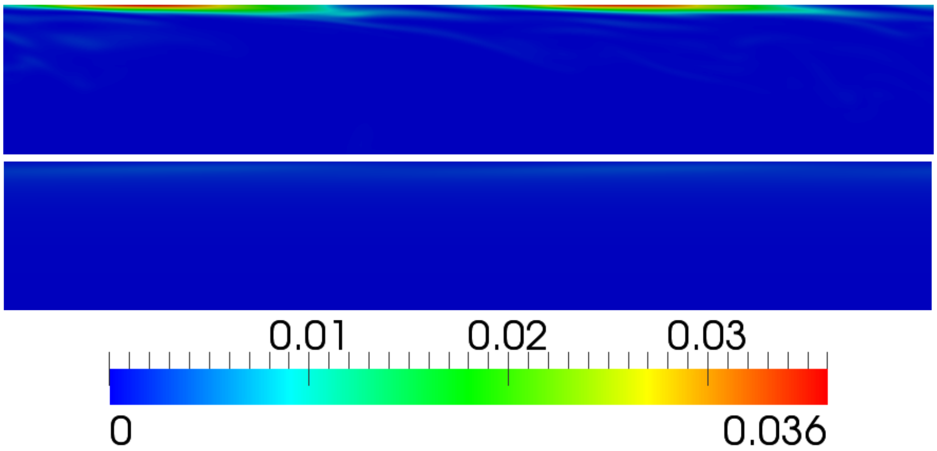

Figure 5.22: Qualitative comparison between a section of the turbulent dissipation field ϵ^* calculated with DNS (top) and the averaged one $\langle\epsilon^*\rangle_{zt}$ calculated with Launder Sharma $k-\epsilon$ model (bottom).

however the comparison is only qualitative because the SSL calculated with DNS is not averaged along the homogeneous direction z and time t.

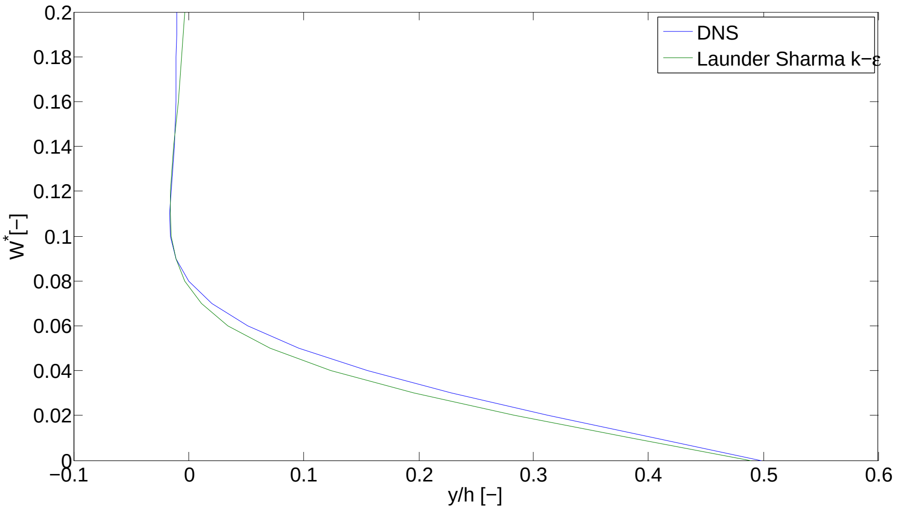

Figure 5.23: Qualitative comparison between the SSL calculated with DNS and the one calculated with Launder Sharma $k-\epsilon$ model.

Chapter 6

Conclusions and Future Works

This work investigates the ability of existing RANS turbulent models to describe skin-friction drag reduction effects generated by a wall based steady forcing. RANS simulations of a channel flow are implemented with the software OpenFOAM using two different turbulence models, i.e. the Launder Sharma $k - \epsilon$ and $\overline{v^2} - f$.

Both the turbulence models considered can predict drag reduction, in fact notwithstanding the results are quantitatively inaccurate, the values of the skin friction coefficient C_f achieved when the control is actuated are lower than the ones calculated in the reference case.

The statistics of the energy balances of the mean and fluctuating flow field are investigated with the aim to understand how the mechanism of drag reduction is included by the turbulence models. In these equations most of the terms are found to be null or negligible as direct consequence of the simplicity of geometry and forcing. The sum of these balances, once averaged over the homogeneous directions z, t and over the direction x and integrated over the direction y, leads to the global balance for total kinetic energy where the viscous dissipation ϵ is found to be an important quantity deeply involved in the modelling and directly affected by the forcing. An analysis of how and why the control acts on this modelled quantity is thus carried on, revealing that the production of ϵ is the term of the equation that mainly changes because of the forcing. It is composed by the sum of two terms: one of them directly affected by the forcing, the other indirectly.

The results obtained with the RANS simulations are compared with the ones achieved via DNS in order to make a quantitative analysis. In the reference case the percentage error made is restrained, whereas in the controlled case it is significant. The ϵ fields calculated with the turbulence models are quantitatively inaccurate. However, the ϵ field calculated with the $\overline{v^2} - f$, when represented on the proper scale, shows an evident modulation in the x direction that is expected, even though some differences exist with reference to the DNS data: the maximum value is not found on the wall but next to it and the elongations in the streamwise flow direction observed in the DNS do not appear.

In this work a constant mass flow rate is imposed, thus the drag reduction manifest itself as a decrease of the wall shear stress. A different choice consists of dictating a constant pressure gradient, so that drag reduction leads to a increase of the bulk velocity U_b. The turbulence model parameters used, are not adjusted for the specific problem, they are in fact the original ones. Most importantly, the Boussinesq hypothesis could be not suitable for the study of these phenomena, characterized by a complex physics. This work should be regarded as preliminary. Indeed, our interest lies in the characterization of Reynolds Stress Transport Model (RSTM)-type models when applied to the present problem. The RSTM models, although more complex, should allow to better describe the complex physics behind turbulent skin-friction drag reduction. In particular the interaction between pressure and strain, which is believed [35] to play a central role in the spanwise forcing, is explicitly described by RSTM. The present work results, although still qualitatively unsatisfactory, are promising this respect.

Bibliography

[1] R. Akhavan, W. Jung, and N. Mangiavacchi. Control of wall turbulence by high frequency wall oscillations. *AIAA Paper 93-3282*, 1993.

[2] F. Auteri, A. Baron, M. Belan, G. Campanardi, and M. Quadrio. Experimental assessment of drag reduction by traveling waves in a turbulent pipe flow. *Phys. Fluids*, 22(11):115103/14, 2010.

[3] A. Baron and M. Quadrio. Turbulent drag reduction by spanwise wall oscillations. *Appl. Sci. Res.*, 55:311–326, 1996.

[4] M. Belan and M. Quadrio. A perturbative model for predicting the high-reynolds-number behaviour of the streamwise travelling waves technique in turbulent drag reduction. *ZAMM.*, 93(12):944–962, 2013.

[5] T. W. Berger, J. Kim, C. Lee, and J. Lim. Turbulent boundary layer control utilizing the Lorentz force. *Phys. Fluids*, 12(3):631–649, 2000.

[6] P. Bradshaw and N.S. Pontikos. Measurements in the turbulent boundary layer on an ‘infinite’ swept wing. *J. Fluid Mech.*, 159:105–130, 1985.

[7] J.-I. Choi, C.-X. Xu, and H. J. Sung. Drag reduction by spanwise wall oscillation in wall-bounded turbulent flows. *AIAA J.*, 40(5):842–850, 2002.

[8] K-S. Choi, J.R. DeBisschop, and B.R. Clayton. Turbulent boundary-layer control by means of spanwise-wall oscillation. *AIAA J.*, 36(7):1157–1162, 1998.

[9] K-S. Choi and M. Graham. Drag reduction of turbulent pipe flows by circular-wall oscillation. *Phys. Fluids*, 10(1):7–9, 1998.

[10] Y. M. Chung and E. Hurst. *Turbulent drag reduction at high Reynolds numbers. In Fluid-Structure-Sound Interactions and Control.* Springer, 2013.

[11] Nielsen P.V. Davidson, L. and Sveningsson A. Modifications of the v2-f model for computing the flow in a 3d wall jet. *Turbulence, Heat and Mass Transfer*, 4:577–584, 2003.

[12] Y. Du and G. E. Karniadakis. Suppressing wall turbulence by means of a transverse traveling wave. *Science*, 288:1230–1234, 2000.

[13] Y. Du, V. Symeonidis, and G. E. Karniadakis. Drag reduction in wall-bounded turbulence via a transverse travelling wave. *J. Fluid Mech.*, 457:1–34, 2002.

[14] C.A. Duque-Daza, M.F. Baig, D.A. Lockerby, S.I. Chernyshenko, and C. Davies. Modelling turbulent skin-friction control using linearised Navier-Stokes equations. *J. Fluid Mech.*, xxx, 2012.

[15] P.A. Durbin. Near-wall turbulence closure modeling without "damping functions". *Theoret. Comput. Fluid Dynamics*, 3:1–13, 1991.

[16] R. Garcia-Mayoral and J. Jiménez. Drag reduction by riblets. *Phil. Trans. R.Soc. A*, 369(1940):1412–1427, 2011.

[17] D. Gatti and M. Quadrio. Performance losses of drag-reducing spanwise forcing at moderate values of the reynolds number. *Phys. Fluids*, 25:125109–17, 2013.

[18] S. Hoyas and J. Jiménez. Reynolds number effects on the reynolds-stress budgets in turbulent channels. *Phys. Fluids*, 20:101511–8, 2008.

[19] J. Jeong and F. Hussain. On the identification of a vortex. *J. Fluid Mech.*, 285:69–94, 1995.

[20] W.P. Jones and Launder B.E. The prediction of laminarization with a two-equation model of turbulence. *International Journal of Heat and Mass Transfer*, 15:301–314, 1972.

[21] W.J. Jung, N. Mangiavacchi, and R. Akhavan. Suppression of turbulence in wall-bounded flows by high-frequency spanwise oscillations. *Phys. Fluids A*, 4 (8):1605–1607, 1992.

[22] N. Kasagi, Y. Hasegawa, and K. Fukagata. Towards cost-effective control of wall turbulence for skin-friction drag reduction. volume 132 of *Advances in Turbulence XII*, pages 189–200. Springer, 2009.

[23] J. Kim and F. Hussain. Propagation velocity of perturbations in turbulent channel flow. *Phys. Fluids A*, 5(3):695–706, 1993.

[24] B.E. Launder and B.I. Sharma. Application of the energy-dissipation model of turbulence to the calculation of flow near a spinning disc. *Letters in heat and mass transfer*, 1:131–138, 1974.

[25] F.S. Lien and G. Kalitzin. Computations of transonic flow with the v2-f turbulence model. *International Journal of Heat and Fluid Flow*, 22:53–61, 2001.

[26] P. Luchini and M. Quadrio. A low-cost parallel implementation of direct numerical simulation of wall turbulence. *J. Comp. Phys.*, 211(2):551–571, 2006.

[27] R. Moarref and M.R. Jovanovic. Model-based design of transverse wall oscillations for turbulent drag reduction. *Journal Fluid Mech.*, 707:205–240, 2012.

[28] J. Pang and K.-S. Choi. Turbulent drag reduction by Lorentz force oscillation. *Phys. Fluids*, 16(5):L35–L38, 2004.

[29] Rodi W. Patel, V.C. and Scheuerer G. Turbulence models for near-wall and low reynolds number flows: a review. *AIAA Journal*, 23:1308–1319, 1985.

[30] S.B. Pope. *Turbulent Flows.* Cambridge University Press, Cambridge, 2000.

[31] M. Quadrio. Drag reduction in turbulent boundary layers by in-plane wall motion. *Phil. Trans. R. Soc. A*, 369(1940):1428–1442, 2011.

[32] M. Quadrio and P. Ricco. Critical assessment of turbulent drag reduction through spanwise wall oscillation. *J. Fluid Mech.*, 521:251–271, 2004.

[33] M. Quadrio and P. Ricco. The laminar generalized Stokes layer and turbulent drag reduction. *J. Fluid Mech.*, 667:135–157, 2011.

[34] M. Quadrio, P. Ricco, and C. Viotti. Streamwise-traveling waves of spanwise wall velocity for turbulent drag reduction. *J. Fluid Mech.*, 627:161–178, 2009.

[35] Ottonelli C. Ricco, P., Hasegawa Y. Jiménez, J., and M. Quadrio. Changes in turbulent dissipation in a channel flow with oscillating walls. *J. Fluid Mech.*, 700:77–104, 2012.

[36] P. Ricco and M. Quadrio. Wall-oscillation conditions for drag reduction in turbulent channel flow. *Intl J. Heat Fluid Flow*, 29:601–612, 2008.

[37] S. Tamano and M. Itoh. Drag reduction in turbulent boundary layers by spanwise traveling waves with wall deformation. *J. Turbulence*, 13, 2012.

[38] E. Touber and M.A. Leschziner. Near-wall streak modification by spanwise oscillatory wall motion and drag-reduction mechanisms. *J. Fluid Mech.*, 693:150–200, 2012.

[39] E.R. Van Driest. On turbulent flow near a wall. *Journal of the Aeronautical Sciences*, 23:1007–1011, 1956.

[40] C. Viotti, M. Quadrio, and P. Luchini. Streamwise oscillation of spanwise velocity at the wall of a channel for turbulent drag reduction. *Phys. Fluids*, 21:115109, 2009.

[41] P.R. Viswanath. Aircraft viscous drag reduction using riblets. *Prog. Aerosp. Sci.*, 38:571–600, 2002.

[42] D.C. Wilcox. *Turbulence modelng for CFD.* Birmingham Press, 3nd edition, 2006.

[43] W Xie and M. Quadrio. Wall turbulence control by spanwise-traveling waves. *European Turbulence Conference*, ENS Lyon, Sep 2013.

[44] H. Zhao, J.-Z. Wu, and J.-S. Luo. Turbulent drag reduction by traveling wave of flexible wall. *Fluid Dyn. Res.*, 34:175–198, 2004.